Spectroscopy and structure of hibonite, grossite, and $CaAl_2O_4$: Implications for astronomical environments

ANNE M. HOFMEISTER,[1],* BRIGITTE WOPENKA,[1] and ANDREW J. LOCOCK[2]

[1]Department of Earth and Planetary Sciences, Washington University, St. Louis, MO 63130, USA
[2]Department of Civil Engineering and Geological Sciences, University of Notre Dame, Notre Dame, IN 46556, USA

Abstract—Infrared (IR) spectra of phases found in calcium-aluminum rich inclusions in meteorites are incomplete, yet such data are needed to ascertain the mineralogy of astronomical environments. To better characterize the system $CaO-Al_2O_3$, we obtained IR thin-film absorption data, partially polarized Raman scattering spectra, and single-crystal X-ray structure refinements from small single-crystals of end-member hibonite ($CaAl_{12}O_{19}$) and grossite ($CaAl_4O_7$), synthesized by laser-heating. Vibrational spectra were also acquired from natural samples of Th-bearing hibonite, synthetic corundum (Al_2O_3), ^{17}O-enriched grossite, $CaAl_2O_4$, and CaO. Spectral fitting provided band positions and widths. The true absorbance of strong IR peaks in calcium aluminates is $1-2/\mu m$, based on thickness determined from interference fringes and on comparison with absorption coefficients calculated from reflectivity data on natural hibonite. Our data on the lattice vibrations of hibonite reveal that the terrestrial samples are partially metamict: their spectra cannot be used for comparison with astronomical objects because of peak broadening and changes in the polarization of the vibrations.

Direct comparison of our IR data of synthetic samples with astronomical observations shows that grossite and hibonite are present in the proto-planetary nebula NGC 6302. That spectral patterns match provides a strong case. Corundum, spinel, and melilite-group minerals also could be present in the nebula. Because spectra of melilites resemble those of pyroxenes, the latter assignment is less certain. We limit our compositional analysis of the nebula to matching spectral patterns, because detailed spectral modeling of the mineralogy would be both premature (due to a lack of cryogenic IR data), and uncertain (due to the occurrence of dust in clumps large enough to emit as blackbodies). The inferred mineralogy of NGC 6302 follows the condensation sequence for a nebula of solar composition, and contains mineral types known to be presolar. *Copyright © 2004 Elsevier Ltd*

1. INTRODUCTION

Calcium-aluminum rich inclusions (CAIs) in primitive chondritic meteorites contain most of the phases in the system $CaO-Al_2O_3$ (Brearley and Jones, 1998). Corundum (Al_2O_3) is found in carbonaceous chondrites (Greshake et al., 1996); hibonite ($CaAl_{12}O_{19}$) exists in enstatite, ordinary, and carbonaceous chondrites (Keil and Fuchs, 1971; Bischoff et al., 1985); grossite ($CaAl_4O_7$) occurs in carbonaceous chondrites (Christophe et al., 1982; Paque, 1987; Weber and Bischoff, 1994); and $CaAl_2O_4$ was recently discovered in a grossite-rich CAI from a carbonaceous chondrite (Ivanova et al., 2002). These phases condensed from the primitive, early solar nebula. Isotopic evidence for the former existence of short lived radionuclei in hibonite grains suggests that CAIs represent some of the first solids to form (Grossman, 1980; Podosek and Cassen, 1994; MacPherson et al., 1995). Moreover, some corundum and hibonite grains predate our solar system (Huss et al., 1994; Nittler et al., 1994; Choi et al., 1999).

Previous identification of CAI phases in space through comparison of astronomical spectra with laboratory data is equivocal. Corundum has been inferred (Sloan et al., 2003), but alternative assignments exist (e.g., Speck et al., 2000). Observational data are not the limiting factor, as the Infrared Space Observatory (ISO) has provided unprecedented high-resolution mid and far-IR spectra of a variety of astronomical objects (e.g., Waters, 2000; Salama et al., 2000). Rather, available IR spectra of calcium-aluminates are insufficient for the task.

Corundum, grossite, and $CaAl_2O_4$ from CAIs have near end-member chemical compositions (Weber and Bischoff, 1994; Greshake et al., 1996; Ivanova et al., 2002). Because meteoritic hibonite contains substantial substitution of Mg, Fe, and Ti (Keil and Fuchs, 1971; Bischoff et al., 1985), terrestrial samples have been substituted in experiments (Floss et al., 1998). However, Madagascar hibonite contains large amounts (~wt.% levels) of rare earth elements (REEs), and Th (Bermanec et al., 1996; Floss et al., 1998). Laser-induced photoluminescence associated with REEs affects Raman measurements (Burruss et al., 1992; Wopenka et al., 1996). High concentrations of Th cause α-particle damage, leading to a partially metamict structure that is not expected to occur in extraterrestrial minerals. For example, radiation damage in zircon occurs at trace levels of Th (or U) and is known to alter spectroscopic properties, due to short-range changes in the crystal structure (Woodhead et al., 1991; Murakami et al., 1991; Weber et al., 1994; Nasdala et al., 1995; Wopenka et al., 1996; Rios et al., 2000). Determining the degree of metamictization is needed to evaluate if Madagascar samples are suitable analogues for extraterrestrial hibonite.

This paper describes a new method for synthesizing calcium-aluminates, and characterizes our products using IR, Raman,

* Author to whom correspondence should be addressed (hofmeist@levee.wustl.edu).

and X-ray diffraction (XRD) techniques. Single-crystal, high-quality, X-ray refinements are used to identify the structure of the small synthetic samples and accurately compare samples with different chemical compositions. We obtained IR data from thin films because this technique provides absorption coefficients close to ideal. Our spectral characterization is as complete as possible in lieu of having large single-crystals. In a companion paper, the spectral parameters are used to calculate thermal properties for the system $CaO-Al_2O_3$ (Hofmeister, in press). In the present study, our data are used to infer the mineralogy of proto-planetary nebula NGC 6302 through pattern identification. We show that these refractory minerals are more likely present than calcite as was previously suggested (Kemper et al., 2002).

2. SAMPLES

2.1. Natural Hibonite

We examined two samples of natural hibonite from the type locality at Esiva, Fort Dauphin region, Madagascar (Curien et al., 1956). Infrared reflectance, absorbance, and Raman scattering were obtained from a cm-sized crystal from the Washington University collection, denoted "black hibonite." A second natural sample, "brown hibonite," consisting of mm-size clove-brown crystals on matrix, was purchased from Le Mineral Brut of Ambronay, France. The same brown single-crystal was studied by Raman and crystallographic techniques and analyzed by electron microprobe. IR data were obtained from a different grain from the same specimen.

2.2. Purchased and Loaned Synthetics

Powdered materials used for spectroscopy or as raw material for syntheses, are calcium monoaluminate, $CaAl_2O_4$ (purity 99% from Alfa/Aesar), CaO (purity 99.99% from Alfa/Aesar), and Al_2O_3 (purity 99.2% from Baker). The lime was dehydrated before use. Isotopically doped grossite ($CaAl_4O_7$) provided by J. Stebbins was used for IR thin-film measurements. For synthesis procedures, description, and nuclear magnetic resonance characterization, see Stebbins et al. (2001).

2.3. Additional Samples Needed for Comparison to NGC 6302

IR data were collected from synthetic forsterite (Mg_2SiO_4, samples from Alfa/Aesar), Mg-rich enstatite ($Mg_{1.94}Fe_{0.06}SiO_3$) from Webster, Jackson, N. Carolina, nearly end-member diopside [$CaMg_{0.97}Fe_{0.03}(SiO_3)_2$] from DeKalb, New York, synthetic gehlenite [$CaAl(AlSi)O_7$] and akermanite ($Ca_2MgSi_2O_7$) (Charlu et al., 1981), melilite (essentially 55% gehlenite and 34% akermanite with 2.0 wt.% FeO and 3.4 wt.% Na_2O) from Iron Hill Complex, Colorado, essentially end-member spinel ($MgAl_2O_4$) from Ceylon, and essentially pure calcite (locality unknown). Chemical analyses of samples from these localities exist in the literature (e.g., Deer et al., 1978).

2.4. Synthesis Procedures

Stoichiometric amounts either of Al_2O_3 and $CaAl_2O_4$, or of Al_2O_3 and CaO, in batches of ~200 mg total weight, were mixed in a ceramic mortar. No special effort was made to obtain homogeneous mixtures. Samples were pressed into pellets, ~7 mm diameter by 2 mm thick, and placed on molybdenum or tungsten foils or tungsten wire gauze inside a vacuum chamber of our own design. A focussed CO_2 laser with 200 W maximum power was rastered across the disk. A simple lens was used to view the sample during heating. Some spots were heated until melting occurred, as indicated by the formation of small spheres or by the fluidity of the material. Different laser powers and heating times were used. Selected run products were characterized using IR, Raman, and XRD techniques. Subsequent to laser-heating, some of the run products from oxide mixtures were heated in air at 1273 K for 92 h.

Using CaO as a starting material produced a mixture of phases regardless of whether laser-heating alone was used, or laser-heating and subsequent annealing were undertaken. Sub-millimeter spheres were almost entirely grossite, apparently a result of incongruent melting. Crystals of hibonite sometimes radiated from the melted regions. A single-crystal of hibonite ~200 μm in length was extracted for structure refinement and Raman measurements.

When $CaAl_2O_4$ was used as a starting material, masses of small grossite crystals were obtained. In a laser-heating run, two needles of grossite extruded from a mat of intergrown needles. A single crystal, $10 \times 10 \times 260$ μm^3, was used for crystallographic refinement.

3. MATERIAL AND METHODS

3.1. Electron Microprobe Analysis

Floss et al. (1998) report chemical analysis of black hibonite. For brown hibonite, wavelength dispersive analyses were obtained from crystals in a thin section and also from the very grain studied with XRD and Raman techniques using a JEOL-733 electron microprobe equipped with Advanced Microbeam automation. The accelerating voltage was 15 kV, the beam current was nominally 30 nA, and the beam diameter was 1 μm for all spots. Silicates, oxides, and REE orthophosphates (Jarosewich and Boatner, 1991) were used as primary standards. La, Ce, and Nd were measured for 60 s on peak using Lα lines and an LiF crystal, and Y was measured (as a proxy for the heavy REE) using the Lα line and a pentererithryhtol (PET) crystal: REE glasses (Drake and Weill, 1972) provided a cross-check. Backgrounds were measured and subtracted for all elements. For brown hibonite, Y concentrations were below detection, providing a firm lower limit for heavy REE concentrations which is consistent with extrapolation from light to heavy REE on a chondrite-normalized plot. Thorium was measured using a ThO_2 standard, Mα line, and a PET crystal. Elements Mn and Zr (on PET, Lα), and Hf (LiF, Lα) were below detection limits (<0.15 wt.%) for 60-s counts at 30 nA. X-ray matrix corrections were based on a modified Armstrong (1988) CITZAF routine. The largest crystal in the thin section is zoned (Table 1). The compositions (Table 1) resemble those of black hibonite (Floss et al., 1998), but our brown hibonite has lower Fe and Ti contents, consistent with its lighter color.

3.2. Single-crystal X-ray Diffraction

3.2.1. Data collection

Synthetic grossite and hibonite as well as the natural clove-brown hibonite were examined. Each single-crystal was mounted on a Bruker PLATFORM three-circle X-ray diffractometer operated at 50 keV and 40 mA, and equipped with a 4K APEX charge-coupled device (CCD) detector and a crystal to detector distance of ~4.7 cm. A sphere of three-dimensional data was collected at room temperature for each crystal using graphite-monochromated MoKα X-radiation and frame widths of 0.3° in ω, with count-times per frame of 20 s for synthetic hibonite, 5 s for natural hibonite, and 60 s for synthetic grossite.

Table 1. Electron microprobe analysis of natural, clove-brown hibonite.[a]

Wt.% oxides	Core	Intermediate	Rim	Crystal[b]
Al_2O_3	76.4	78.8	77.6	78.5 ± 0.5
CaO	7.23	6.67	5.61	6.02 ± 0.2
TiO_2	5.81	4.48	3.04	3.24 ± 0.2
FeO	2.44	2.32	2.21	2.16 ± 0.1
MgO	2.96	2.83	2.72	2.75 ± 0.05
SiO_2	0.75	0.64	0.51	0.52 ± 0.03
Ce_2O_3	0.24	2.96	3.90	2.59 ± 0.3
La_2O_3	0.12	1.47	1.94	1.59 ± 0.2
Nd_2O_3	0.02	0.31	0.40	0.23 ± 0.1
ThO_2	0.09	0.39	0.39	0.37 ± 0.08
Total	96.4	100.9	98.6	98.1 ± 0.6
No. of points	3	2	2	30

[a] Mn, Hf, Y, and Zr are below the limits of detection. For comparison, end-member hibonite has 8.4 wt.% CaO plus 91.6 wt.% Al_2O_3. Metamict samples are often hydrated, which seems to be reflected in the totals being slightly low.
[b] Crystal denotes the sample used for XRD and Raman studies. Core, intermediate, and rim analyses were obtained from a different crystal in thin section. The ranges suggest possible compositions for the grain used for IR measurements.

Comparison of the intensities of equivalent reflections measured at different times during data collection showed no significant decay for any of the three samples. The unit cells (Table 2) were refined using least-squares techniques and 2094 reflections for synthetic hibonite, 3799 reflections for natural hibonite, and 1000 reflections for synthetic grossite. The intensity data were reduced and corrected for Lorentz, polarization, and background effects using the program SAINT (Bruker, 1998a). Semiempirical corrections for absorption were applied using XPREP (Bruker, 1998b) and modeling the crystal as ellipsoids. The space group $P6_3/mmc$ was assigned to hibonite, in accord with previous structure refinements (Bermanec et al., 1996; Utsunomiya et al., 1988; Kato and Saalfeld, 1968). The space group $C2/c$ was assigned to synthetic grossite, after Weber and Bischoff (1994), Goodwin and Lindop (1970), and Ponomarev et al. (1970). Scattering curves for neutral atoms, together with anomalous dispersion corrections, were taken from Ibers and Hamilton (1974). The SHELXTL Version 5 (Bruker, 1998c) series of programs was used for the solution and refinement of the crystal structures.

3.2.2. Crystal structure refinement

For hibonite, the atomic positions of Utsunomiya et al. (1988) were used as a starting point. The structure models, including anisotropic displacement parameters for all atoms converged, giving an agreement index ($R1$) of 2.7% for synthetic hibonite, calculated for the 445 observed unique reflections ($F_o \geq 4\sigma_F$). For natural hibonite, $R1$ is 3.0%, calculated for the 487 observed unique reflections ($F_o \geq 4\sigma_F$). The total scattering-power of the cation sites (Hawthorne et al., 1995) in natural hibonite was refined; the Ca(1), Al(2), and Al(4) sites refined to site scattering values (electrons per formula unit) of 28.0(1), 13.5(1), and 13.6(1) epfu respectively, whereas the Al(1), Al(3), and Al(5) sites did not show detectable variation from 13 epfu. Our refinements are in excellent agreement with results for other hibonite samples (Bermanec et al., 1996; Utsunomiya et al., 1988; Kato and Saalfeld, 1968).

For grossite, the atomic positions of Goodwin and Lindop (1970) were used as a starting point. The model, including anisotropic displacement parameters for all atoms, converged, giving $R1$ of 2.8%, calculated for the 880 observed unique reflections ($F_o \geq 4\sigma_F$). Our

Table 2. Crystallographic data and details of the XRD structure refinements.[a]

Compound	Synthetic hibonite	Natural hibonite	Synthetic grossite
a (Å)	5.5655(8)	5.5853(2)	12.876(1)
b (Å)			8.8781(7)
c (Å)	21.923(4)	22.090(1)	5.4404(4)
β(°)			106.831(2)
V (Å³)	588.1(1)	596.8(1)	595.3(1)
Space group	$P6_3/mmc$	$P6_3/mmc$	$C2/c$
Z	2	2	4
Ideal formula	$CaAl_{12}O_{19}$	$CaAl_{12}O_{19}$	$CaAl_4O_7$
Formula weight (g/mol)[b]	667.85	667.85	260.00
λ(Å)-Mo$K\alpha$	0.71073	0.71073	0.71073
Temperature (K)	293(2)	293(2)	293(2)
$F(000)$[b]	656	656	512
μ (mm^{-1})[b]	1.58	1.56	1.64
D_{calc} (g/mL)[b]	3.772(1)	3.716(1)	2.901(1)
Crystal size (mm³)	0.18 × 0.15 × 0.04	0.30 × 0.20 × 0.10	0.01 × 0.01 × 0.26
2θ range	7.4–68.9°	7.4–69.0°	5.7–69.0°
Completeness $2\theta = 69°$	99.6%	99.8%	97.9%
Data collected	h ± 8, k ± 8, l ± 34	h ± 8, k ± 8, −35 ≤ l ≤ 34	h ± 20, k ± 14, l ± 8
Total reflections	11,151	11,227	5961
Unique reflections, R_{int}	535, 10.0%	544, 5.5%	1250, 5.3%
Unique $|F_o| \geq 4\sigma_F$	445	487	880
Parameters varied	42	45	56
$R1$[c] for $|F_o| \geq 4\sigma_F$	2.7	3.0	2.8
$R1$[c] all data, wR_2[d]	3.5, 8.6	3.5, 9.0	5.0, 5.8
Weighting a, b	0.0255, 0.653	0.042, 0.8227	0.0196, 0
Goodness of fit all data	1.303	1.148	0.827
Max. min. peaks (e/Å³)	0.48, −0.47	0.83, −0.57	0.52, −0.39

[a] For all crystals, a semi-empirical ellipsoid was used for the absorption correction, and the refinement method was full-matrix least squares on F^2. The same clove brown sample was used for Raman measurements, likewise for the synthetic hibonite.
[b] Calculated with ideal occupancy of all atomic positions.
[c] $R1 = [\Sigma||F_o| - |F_c||]/\Sigma|F_o|] \times 100$.
[d] $wR_2 = [\Sigma[w(F_o^2 - F_c^2)^2]/\Sigma[w(F_o^2)^2]]^{0.5} \times 100$, $w = 1/[\sigma^2(F_o^2) + (aP)^2 + bP]$, $P = 1/3 \max(0, F_o^2) + 2/3 F_c^2$.

Table 3. Atomic coordinates ($\times 10^4$) and displacement parameters ($\text{Å}^2 \times 10^3$) for synthetic hibonite.[a]

	x	y	z	U_{eq}	U_{11}	U_{22}	U_{33}	U_{23}	U_{13}	U_{12}
Ca (1)	6667	3333	2500	16 (1)	15 (1)	15 (1)	18 (1)	0	0	7 (1)
Al (1)	0	0	0	5 (1)	5 (1)	5 (1)	5 (1)	0	0	3 (1)
Al (2)[b]	0	0	2577 (4)	9 (2)	5 (1)	5 (1)	18 (5)	0	0	2 (1)
Al (3)	3333	6667	282 (1)	5 (1)	5 (1)	5 (1)	7 (1)	0	0	2 (1)
Al (4)	3333	6667	1909 (1)	6 (1)	5 (1)	5 (1)	7 (1)	0	0	2 (1)
Al (5)	1684 (1)	3369 (2)	−1091 (1)	6 (1)	5 (1)	4 (1)	7 (1)	0 (1)	0 (1)	2 (1)
O (1)	0	0	−1491 (1)	6 (1)	4 (1)	4 (1)	11 (1)	0	0	2 (1)
O (2)	6667	3333	545 (1)	6 (1)	6 (1)	6 (1)	6 (1)	0	0	3 (1)
O (3)	1811 (2)	3622 (5)	2500	8 (1)	10 (1)	5 (1)	9 (1)	0	0	2 (1)
O (4)	1548 (2)	3097 (3)	521 (1)	6 (1)	5 (1)	5 (1)	8 (1)	0 (1)	0 (1)	3 (1)
O (5)	5037 (2)	10073 (3)	1492 (1)	7 (1)	6 (1)	6 (1)	8 (1)	1 (1)	0 (1)	3 (1)

[a] U_{eq} is defined as one-third of the trace of the orthogonalized U_{ij} tensor. The anisotropic displacement parameter exponent takes the form: $-2\pi^2$ [$h^2 a^{*2} U_{11} + \ldots 2 hka^* b^* U_{12}$].
[b] Site is half-occupied and separated from its symmetry equivalent by 0.34(1) Å.

refinement confirms previous results (Goodwin and Lindop, 1970; Ponomarev et al., 1970).

Atomic positional parameters and displacement parameters of synthetic hibonite, natural hibonite, and synthetic grossite are given in Tables 3–5 respectively. Selected interatomic distances for synthetic and natural hibonite are in Table 6. Table 7 lists selected interatomic distances for synthetic grossite. Observed and calculated structure factors along with interatomic angles for these three compounds have been deposited with the editorial office of *Geochimica et Cosmochimica Acta*.

3.3. Raman Spectroscopy

Spectra were taken with a laser Raman microprobe. The device is a fiber-optically coupled microscope-spectrometer-detector system from Kaiser Optical Systems, Inc. (Ann Arbor, Michigan). The Nd:YAG frequency-doubled laser emits at 532 nm (18,797 cm^{-1}) with a maximum output of 100 mW. The system consists of an f/1.8 holographic imaging spectrograph, a 2048-channel CCD array detector, and a Leica polarized-light microscope. The lowest peak position that can be observed with the apparatus is ~135 cm^{-1}. The samples were analyzed in the 180° backscattering configuration; the laser spot size was ~1 μm. Spectra were taken from the same spot in both scrambled (unpolarized) and polarized light (the two polarizations are at right angles to each other). The intent of our polarization experiments was to resolve overlapping modes from different symmetries.

3.4. Infrared Spectroscopy

A general description of quantitative IR analysis is provided by Wooten (1972). For detailed descriptions of IR methods relevant to mineralogy, see Hofmeister (1995), Hofmeister and Mao (2001), and Hofmeister et al. (2003, 2004). Here we provide specifics of the experiments, particularly the thin-film method as it is the mainstay of this paper.

To allow others to utilize our data in modeling astronomical environments, the final results (raw reflectivity data, derived functions, and merged and baseline corrected IR thin-film spectra) are deposited with *Geochimica et Cosmochimica Acta* and on the Washington University website (http://epscx.wustl.edu/~irspectra).

3.4.1. Instrumentation and reflectivity measurements

IR spectra were obtained at ambient conditions using an evacuated Bomem DA3.02 Fourier transform interferometer (FTIR) with an SiC globar as the source. Mid-IR data (4000–500 cm^{-1}) were acquired using a liquid N$_2$ cooled HgCdTe detector and a KBr beamsplitter. For the far-IR, we used a liquid He cooled silicon bolometer and a coated 3-μm broadband beamsplitter for 600 to ~100 cm^{-1} or a 12-μm Mylar below ~200 cm^{-1}. For each spectral segment, between 500 to 2000 scans were collected at a resolution of 1 cm^{-1}, except that 2 cm^{-1}

resolution was used for brown hibonite. Note that resolution is the closest spacing that a pair of peaks can have and still be recognized as a doublet, whereas uncertainties in the peak positions are governed by the instrumental accuracy of 0.01 cm^{-1}. A cryostat of our own design was used to obtain spectra of amorphous ice adhering to a polycard at 77 K (liquid nitrogen temperature).

Infrared reflectance spectra of the black hibonite were collected for **E**⊥**c** at near normal incidence, unpolarized, from an **a-a** section of black hibonite using a Spectratech FTIR microscope. The area of the sample with the best polish was selected to obtain accurate reflectivity values. Our method was checked against standards (MgO and α-SiC). Far- and mid-IR regions were scaled to match in the ~450–600 cm^{-1} region, and the segments were merged. The lowest range ($\nu < 100$ cm^{-1}) was similarly merged. Kramers-Kronig analysis (Spitzer et al., 1962, Andermann et al., 1965) was performed on merged spectra for **E**⊥**c** by assuming that R was constant below the range of measurements ($\nu < $ ~40 cm^{-1}). For higher frequencies, we used constant reflectivity rather than the approximation of Wooten (1972) because the data at high frequency seem to be affected by back reflections. Peak positions of the transverse optic (TO) modes and full widths at half maximum (FWHM) are obtained from the peaks in the imaginary part of the dielectric function (ε_2). Longitudinal optic (LO) positions are obtained from the minima in the imaginary part of ($1/\varepsilon$).

For **E** ∥ **c**, data were collected at 30° incidence from an **a-c** section using a specular reflection device and in the s-polarization. Because the entire crystal is sampled, errors in the absolute reflectivity are expected. The data were not quantitatively analyzed (see below).

3.4.2. The thin-film method

Mid and far-IR absorption spectra were collected from thin films made by compressing a few grains or coarsely ground powder in a Mao-Bell diamond-anvil-cell (DAC). The DAC serves as a sample holder, and is interfaced with the spectrometer through use of a beam condensor. Films were compressed until their appearance in a high-power binocular microscope was uniform with no discernable grain-boundaries. These fragile films generally contain a few cracks. Grain boundaries are largely eliminated because (1) shear forces perpendicular to the diamond faces remove the porosity and reduce mismatches between the crystal faces, and (2) the smooth faces of the diamonds themselves strongly limit surface roughness. Consequently, the effect of crystal size on the transmission spectra that is described and modeled in the ceramics literature (e.g., Sulewski et al., 1987; Mayerhöfer, 2002) is mitigated with our technique. The films are optically thin, and thus should closely represent the ideal absorption spectra. Extremely hard minerals such as Al$_2$O$_3$ present difficulties in making smooth, even films, which needs to be taken into account in evaluating the quality of the data.

Interference fringes occur in the mid-IR. Their spacing ($\Delta\nu$) and measurements of the index of refraction (n) in the visible allow inference of the gap between the diamond anvils:

$$d = \frac{1}{2(n^2 - \sin^2 \theta)^{1/2} \Delta v}. \tag{1}$$

Incidence is nearly normal, and using $\theta = 0$ sets an upper limit on the thickness of the mineral film. The uncertainties in d are large enough that accounting for θ in Eqn. 1 is unnecessary. From Gaines et al. (1997), n of grossite is 1.63 (averaged over the various orientations), n of hibonite is 1.80, and n of corundum is 1.76. For $CaAl_2O_4$, we use n of grossite, as the densities (ρ) of these two phases are nearly the same. Note that both n and ρ of hibonite and corundum are similar, but differ considerably from those of grossite.

The absorption spectra shown below are uncorrected. Spectra on deposit (http://epscx.wustl.edu/~irspectra) were processed as follows. After removal of the fringes in the mid-IR by baseline subtraction, the more intense of the far-IR or mid-IR segments was scaled to match the less intense segment, and the data were merged. The final results are recalculated to represent the true absorption coefficient

$$Ad = 2.3026[a_{chem} + 2 \log (1 - R)] \tag{2}$$

where R is reflectivity and

$$a_{chem} = -\log (I_{tra}/I_0) \tag{3}$$

is the measured "chemical" absorbance, generally reported in the mineralogical literature. Because R is unknown for the synthetics, the absorbance was assumed to be nearly zero at the most transparent part of the spectrum, and the corresponding value of R is applied to the remainder of the spectrum. This approach to the baseline poses no problem for weak IR bands, where R varies slowly with frequency (Wooten, 1972). Because the diamond-anvil-cell is used as the reference, most of surface reflections are removed by ratioing the sample throughput to the reference throughput. The procedure creates some errors for diatomics with a single broad, strong IR band (Hofmeister et al., 2003) due to the rapid change in R with v at the sides of the peak. For silicates, good agreement is obtained between thin-film absorption measurements of a and values of A calculated from independent reflectivity measurements of single-crystals. However, the film provides peaks that are more rounded than expected (McAloon and Hofmeister, 1993; Hofmeister, 1995; Hofmeister et al., 2003, 2004). Although peaks for the calcium aluminates are strong, their closely spaced intervals mitigate some of the variations in R with v. Comparing measurements of a with A calculated from reflectivity data on natural hibonite (below) confirms that approximating R as constant for the synthetics is a reasonable approach.

3.4.3. Relationship of emission to reflection and absorption spectra

Dust in astronomical environments can directly absorb IR light from stars more distant. For the object discussed here, and many other cases, the dust is "in emission" (Molster et al., 2001; Kemper et al., 2002), wherein the grains are warmed by absorbing visible light from the star, and release this heat in the form of far-IR to mid-IR light. Speck and Hofmeister (2004) discuss the simple case of emission spectra for SiC.

Emission spectra are related to absorption spectra through Kirchoff's law, i.e., absorptivity equals emissivity. The simplest form is:

$$\xi = 1 - \exp [-dA(v)], \tag{4}$$

where d is the size of the emitting grain in cm, and A is the absorption coefficient in cm^{-1} (Brewster, 1992). The light received (E) is the product of the emissivity and the blackbody function (I) appropriate to the dust grains plus the underlying spectrum of the star:

$$E = \xi I(T). \tag{5}$$

Planck's function is

$$I(v) = \frac{2phv^5}{c^3} \left[\frac{1}{\exp (hcv_B T) - 1} \right] \tag{6}$$

where h is Planck's constant, k_B is Boltzmann's constant, T is temperature, and c is the speed of light. Equation 6 provides the energy-density on a per wavelength basis.

Equations 4 and 5 show that emission spectra are directly related to the intrinsic, true absorption coefficient, which is obtained from quantitative analysis of reflectivity data (Wooten, 1972; Brewster, 1992). As discussed above, the thin-film spectra reasonably represent A for spectral regions with weak peaks. For astronomical data considered here, the far-IR region which contains weak peaks pertains, and the thin-film data can therefore be directly compared to the nebula, given knowledge of film thickness (Eqn. 2). Scattering need not be accounted for, as the nebula is optically thin. We suggest that the shape of the particle is immaterial, because (1) the emissions received constitute the average overall grains, and (2) only the direct line-of-sight is sampled. For sufficiently large grains, the light received is simply the blackbody spectrum.

3.5. Peak Fitting Procedures

Peak fitting routines in Grams/AE version 7 were applied to both Raman spectra and the dielectric functions. Lorentzian peak shapes were used, and these are theoretically expected (Burns, 1990). All peaks and shoulders were visible in the raw data: hidden peaks were not needed to achieve a good match between the raw data and the final fits. Linear baselines were used to account for the fluorescence background in the Raman spectra.

Although IR absorption peak shapes are neither Lorentzian nor Gaussian nor a combination (Wooten, 1972), we tried fitting these with Lorentzian shapes. Our reasoning is that several of our samples have many narrow and closely spaced modes, and in this case the dielectric and absorption functions should be very similar. Fits to the thin-film spectra were excellent for the weak far-IR peaks, but only fair for the strong mid-IR modes, as expected, given the association of large strengths with broad widths and large LO-TO splitting (discussed below). Linear baselines were used in fitting all data.

4. STRUCTURE AND SYMMETRY

4.1. Cation Site Symmetries From Crystal Structure Refinements

Hibonite shares the magnetoplumbite structure-type (Utsunomiya et al., 1988; Bermanec et al., 1996). Calcium occurs in 12-fold coordination (with D_{3h} site symmetry), whereas Al is distributed over three symmetrically independent octahedral sites, one tetrahedral site, and one trigonal bipyramidal site (Tables 3, 4, and 6). Although Al(1) is a relatively regular octahedron (D_{3d} site symmetry), Al(4) is trigonally distorted (C_{3v}), and Al(5) is quite distorted (C_s) (Bermanec et al., 1996). The Al(3) tetrahedron is only slightly distorted (C_{3v} site symmetry). The Al(2) trigonal bipyramid has a formal site symmetry of D_{3h} (Bermanec et al., 1996), but the site is split into two symmetrically equivalent half-occupied positions above and below the equatorial plane of the bipyramid due to displacement of the cation from the site-center (Bermanec et al., 1996; Utsunomiya et al., 1988). The half-occupied pseudotetrahedral cation positions of Al(2) are separated by 0.34(1) Å in synthetic hibonite and by 0.45(1) Å in natural hibonite.

In the grossite structure, Ca occurs in sevenfold coordination (with C_2 site symmetry, pseudo-C_{2v}), whereas Al is distributed over two symmetrically independent tetrahedral sites, both of which are quite distorted (C_1 site symmetry) (Goodwin and Lindop, 1970; Ponomarev et al., 1970). Our results (Tables 5 and 7) corroborate these earlier studies.

Table 4. Atomic coordinates ($\times 10^4$) and displacement parameters ($\text{Å}^2 \times 10^3$) for natural brown hibonite.[a]

	x	y	z	U_{eq}	U_{11}	U_{22}	U_{33}	U_{23}	U_{13}	U_{12}
Ca(1)[b]	6667	3333	2500	20 (1)	21 (1)	21 (1)	17 (1)	0	0	10 (1)
Al(1)	0	0	0	8 (1)	7 (1)	7 (1)	9 (1)	0	0	4 (1)
Al(2)[c]	0	0	2603 (2)	20 (1)	10 (1)	10 (1)	39 (4)	0	0	5 (1)
Al(3)	3333	6667	274 (1)	8 (1)	6 (1)	6 (1)	11 (1)	0	0	3 (1)
Al(4)[d]	3333	6667	1893 (1)	9 (1)	8 (1)	8 (1)	10 (1)	0	0	4 (1)
Al(5)	1681 (1)	3361 (1)	−1077 (1)	9 (1)	7 (1)	6 (1)	13 (1)	0 (1)	0 (1)	3 (1)
O(1)	0	0	−1487 (1)	11 (1)	8 (1)	8 (1)	16 (1)	0	0	4 (1)
O(2)	6667	3333	563 (1)	10 (1)	7 (1)	7 (1)	17 (1)	0	0	3 (1)
O(3)	1805 (2)	3611 (5)	2500	18 (1)	22 (1)	18 (1)	12 (1)	0	0	9 (1)
O(4)	1538 (1)	3076 (3)	523 (1)	10 (1)	9 (1)	11 (1)	12 (1)	−2 (1)	−1 (1)	6 (1)
O(5)	5041 (1)	10083 (3)	1496 (1)	10 (1)	8 (1)	9 (1)	13 (1)	2 (1)	1 (1)	4 (1)

[a] U_{eq} is defined as one-third of the trace of the orthogonalized U_{ij} tensor. The anisotropic displacement parameter exponent takes the form: $-2\pi^2$ [$h^2 a^{*2} U_{11} + \ldots + 2\,hka^* b^* U_{12}$].
[b] Refined site scattering value 28.0(1) epfu.
[c] Refined site scattering value 13.5(1) epfu. Site is half-occupied and separated from its symmetry equivalent by 0.45(1) Å.
[d] Refined site scattering value 13.6(1) epfu.

The structure of $CaAl_2O_4$, refined by Dougill (1957) and Hoerkner and Mueller-Buschbaum (1976), is closely related to that of nepheline, and thus to β-tridymite (Palmer, 1994). All atoms are on the general site, with C_1 site symmetry. Two of the Ca ions sit in distorted octahedra, the third Ca is housed in a lopsided pentagonal pyramid, whereas Al is in six distorted tetrahedral sites that are corner linked in three dimensions. We did not collect single crystal X-ray data for $CaAl_2O_4$ because the crystallite sizes were too small.

4.2. Symmetry Analysis

The character of the atomic sites determines the number, type, and symmetry (polarization) of the vibrational modes (Fateley et al., 1972). Because calcium aluminates are structurally complex, only the simplest kind of symmetry analysis is possible.

End-member hibonite (Table 8) has a large number of vibrational modes, but only a small portion of the total modes are Raman or IR active. The E_{1u} polarization is doubly-degenerate, and these 17 optic modes should dominate unpolarized IR spectra. Typically, strong A_{1g} peaks dominate unpolarized Raman spectra. The T(Ca) mode for E_{2g} should also be seen as this motion is not active in A_{1g}.

Grossite (Table 9) has a modest number of vibrations, but all are active. Each polarization in the IR is singly-degenerate, and all 34 modes could be present in the thin-film measurements as the intensities of the two polarizations are similar. Accidental degen-

eracies likely reduce this number. The breakdown of the Raman modes is identical to the IR modes, so many common features are expected. However, the A_g symmetry is expected to dominate the Raman spectrum, so that roughly 17 modes are expected. Because symmetric vibrations are more intense in the Raman, but asymmetric motions dominate the IR, the differences in patterns indicated in Table 9 should help with band assignments.

The number of modes in $CaAl_2O_4$ is huge (Table 10) due to its low symmetry and large unit cell. Raman and IR modes should have similar frequencies.

Samples with significant amounts of site substitution commonly have more modes than is expected from symmetry. Additional (local) modes are connected with vibrations of the end-members in a solid solution series, such that the intensity of each local mode is proportional to the degree of solid solution (Chang and Mitra, 1968). This two-mode behavior is not connected with loss of symmetry, but instead arises when chemical substitutions involve significant differences in atomic masses, in accord with the harmonic oscillator model.

5. SPECTROSCOPIC RESULTS

5.1. Raman Spectra

5.1.1. Synthetic End-members

Between 20 and 26 distinct Raman peaks are observed for each phase (Tables 11a, 12, and 13), which are roughly evenly

Table 5. Atomic coordinates ($\times 10^4$) and displacement parameters ($\text{Å}^2 \times 10^3$) for synthetic grossite.[a]

	x	y	z	U_{eq}	U_{11}	U_{22}	U_{33}	U_{23}	U_{13}	U_{12}
Ca(1)	0	8093 (1)	2500	10 (1)	10 (1)	11 (1)	9 (1)	0	2 (1)	0
Al(1)	1640 (1)	866 (1)	3030 (1)	8 (1)	8 (1)	8 (1)	7 (1)	0 (1)	2 (1)	1 (1)
Al(2)	1197 (1)	4406 (1)	2409 (1)	8 (1)	8 (1)	8 (1)	9 (1)	−1 (1)	4 (1)	−1 (1)
O(1)	0	5318 (2)	2500	11 (1)	10 (1)	9 (1)	16 (1)	0	7 (1)	0
O(2)	1155 (1)	515 (1)	5655 (3)	10 (1)	12 (1)	11 (1)	10 (1)	2 (1)	5 (1)	3 (1)
O(3)	1187 (1)	2550 (2)	1487 (3)	10 (1)	12 (1)	9 (1)	8 (1)	1 (1)	2 (1)	2 (1)
O(4)	1923 (1)	4436 (2)	5798 (3)	9 (1)	9 (1)	11 (1)	7 (1)	−2 (1)	2 (1)	2 (1)

[a] U_{eq} is defined as one-third of the trace of the orthogonalized U_{ij} tensor. The anisotropic displacement parameter exponent takes the form: $-2\pi^2$ [$h^2 a^{*2} U_{11} + \ldots + 2\,hka^* b^* U_{12}$].

Table 6. Selected interatomic distances (Å) for hibonite.

Synthetic hibonite	Natural brown hibonite
Ca(1)-O(5) 2.7117(16) × 6	Ca(1)-O(5) 2.7181(14) × 6
Ca(1)-O(3) 2.7862(4) × 6	Ca(1)-O(3) 2.7958(1) × 6
<Ca(1)-O> 2.749	<Ca(1)-O> 2.757
Al(1)-O(4) 1.8795(16) × 6	Al(1)-O(4) 1.8835(14) × 6
<Al(1)-O> 1.880	<Al(1)-O> 1.884
Al(2)-O(3) 1.754(2) × 3	Al(2)-O(3) 1.761(2) × 3
Al(2)-O(1) 2.042(10)	Al(2)-O(1) 2.010(5)
[Al(2)-O(1) 2.381(10)]	[Al(2)-O(1) 2.465(5)]
<Al(2)-O> 1.826	<Al(2)-O> 1.823
Al(3)-O(4) 1.7988(16) × 3	Al(3)-O(4) 1.8219(15) × 3
Al(3)-O(2) 1.812(3)	Al(3)-O(2) 1.849(3)
<Al(3)-O> 1.802	<Al(3)-O> 1.829
Al(4)-O(5) 1.8793(17) × 3	Al(4)-O(5) 1.8699(14) × 3
Al(4)-O(3) 1.9577(19) × 3	Al(4)-O(3) 1.9961(18) × 3
<Al(4)-O> 1.919	<Al(4)-O> 1.933
Al(5)-O(5) 1.8086(11) × 2	Al(5)-O(5) 1.8364(9) × 2
Al(5)-O(1) 1.8459(15)	Al(5)-O(1) 1.8614(14)
Al(5)-O(2) 1.9895(17)	Al(5)-O(2) 1.9606(16)
Al(5)-O(4) 2.0003(12) × 2	Al(5)-O(4) 1.9841(11) × 2
<Al(5)-O> 1.909	<Al(5)-O> 1.911

spaced in frequency from the instrument limit of 135 cm^{-1} to 900 cm^{-1}. Synthetic calcium aluminates have many sharp, well-defined peaks, and similar peak positions, but distinct patterns (Fig. 1a). Hibonite has one intense band at 910 cm^{-1}, attributed to symmetric Al-O tetrahedral stretching, and many fairly weak peaks. Grossite has two strong bands at 412 and 909 cm^{-1}, respectively due to symmetric bending and stretching of the AlO_4 tetrahedra, as well as a host of moderately intense peaks. Three strong peaks in the Al-O bending region and many broad peaks characterize $CaAl_2O_4$.

Average FWHMs are needed to calculate thermal conductivity (Hofmeister, in press). Peak widths are generally narrow, on the order of 10 cm^{-1}. That the widest peaks occur in $CaAl_2O$ is attributed to many overlapping peaks, as only 26 of the 126 possibly distinct Raman peaks were observed (Tables 10 and 13). For grossite, 25 of the 36 possibly distinct peaks were observed, and for hibonite, 20 of the 42 possible peaks were observed. We estimate <FWHM> of synthetic hibonite as 9.8 cm^{-1} which excludes the two weak peaks with widths near 20 cm^{-1} (Table 11a). The remaining modes occupy the range of 5.5 to 15.8 cm^{-1}. For grossite, we exclude the weak and broad mode at 837 cm^{-1}. The remaining Raman modes lie in the range of 5.3 to 14.9 cm^{-1} and <FWHM> is 8.9 cm^{-1} (Table 12). Widths for $CaAl_2O_4$ range from 5.9 to 24.7, excluding the very broad highest frequency mode at 879 cm^{-1} (Table 13), which is probably an overtone-combination. The average FWHM is 14.3 cm^{-1}.

5.1.2. Natural hibonite

Few, weak Raman peaks were seen for natural hibonite (Fig. 1b). The intensity rises steeply towards high Δcm^{-1}, due to laser-induced photoluminescence. Black and brown hibonite share spectral features, but the resemblance to synthetic hibonite is faint. The most intense peaks in each of the samples were presumed to have the same origin. The linkage is obvious for the strongest mode (Fig. 1b), but is equivocal for all others. Table 11a lists a possible correlation.

5.1.3. Fluorescence spectra

Synthetic hibonite and grossite have laser-induced photoluminescence features around 14,500 absolute cm^{-1}, which are observed near 4000 Δcm^{-1} given our excitation at 18,797 absolute cm^{-1}. The patterns of distinct and narrow peaks superimposed on a fluorescence background (Fig. 2a) differ from each other, but share features with the spectrum of Cr^{3+} ions in ruby. The different coordination of Al in hibonite and grossite produces two distinct Cr^{3+} patterns. Chromium ions are inferred to be an impurity in the Al_2O_3 starting material, because our purchased sample of $CaAl_2O_4$ did not exhibit fluorescence spectra.

5.2. IR Absorption Spectra of Thin Films

5.2.1. Synthetic samples

All three synthetic calcium aluminates have large numbers of closely spaced peaks, occurring in distinct patterns (Fig. 3). The results corroborate previous measurements of hibonite and grossite in KBr dispersions (Mutschke et al., 2002), but cover a wider frequency range (Fig. 3b,c). In accord with symmetry analysis, the number of observed peaks increases in the order hibonite $\rightarrow$ grossite $\rightarrow$ $CaAl_2O_4$, and more IR than Raman peaks are observed for grossite and $CaAl_2O_4$ (Tables 11 to 13). For all phases, the far-IR bands, which are typically translations and rotations-librations, are considerably weaker than the mid-IR modes, which are due to stretching and bending of the tightly-bound units (AlO_4 tetrahedra for these phases). The lowest peak position observed (88 $\rightarrow$ 75 $\rightarrow$ 68 cm^{-1} in the order $CaAl_{12}O_{19} \rightarrow CaAl_4O_7 \rightarrow CaAl_2O_4$) correlates with the increasing proportion of Ca relative to Al. The peak positions of the Al-O tetrahedral stretches (Tables 11 to 13) are connected with polymerization, much as in silicates (Farmer and Lazarev, 1974). Specifically, Al-O stretching modes in grossite (which has ribbons of tetrahedra) have higher frequencies than those in $CaAl_2O_4$ (which has a 3-dimensional network), which are higher than those of hibonite (which has long Al-O bonds).

IR spectra of lime and corundum have fewer and broader bands (Fig. 3d). Rocksalt structures have only one, triply degenerate IR mode. The main peak in the IR spectra of CaO is near the TO position, with a shoulder near the LO. Scaling the

Table 7. Selected inter-atomic distances (Å) for synthetic grossite.

Ca(1)-O(3) 2.3339(14) × 2
Ca(1)-O(2) 2.3687(14) × 2
Ca(1)-O(1) 2.463(2)
Ca(1)-O(2) 2.8813(15) × 2
<Ca(1)-O> 2.519
Al(1)-O(3) 1.7311(15)
Al(1)-O(2) 1.7454(15)
Al(1)-O(2) 1.7593(15)
Al(1)-O(4) 1.7934(14)
<Al(1)-O> 1.757
Al(2)-O(3) 1.7209(15)
Al(2)-O(1) 1.7542(11)
Al(2)-O(4) 1.7815(14)
Al(2)-O(4) 1.8101(15)
<Al(2)-O> 1.767

Table 8. Symmetry analysis of $CaAl_{12}O_{19}$ hibonite (D_{6h}^4 with Z = 2 and 192 total vibrations).

Atom	Site	Symmetry	Raman A_{1g}	-A_{2g}	-B_{1g}	-B_{2g}	Raman E_{1g}	Raman E_{2g}	A_{1u}	-A_{2u}	-B_{1u}	-B_{2u}	IR E_{1u}	-E_{2u}
Ca	2d	$2dD_{3h}''$ (2)	0	0	1	0	0	1	0	1	0	0	1	0
Al(1)	2a	D_{3d}' (2)	0	0	0	0	0	0	0	1	0	1	1	1
Al(2)	2b	D_{3h}'' (2)	0	0	1	0	0	1	0	1	0	0	1	0
Al(3,4)	2 × 4f	$2 \times C_{3v}^d$ (4)	2	0	0	2	2	2	2	0	0	2	2	2
Al(5)	12k	C_s^d (12)	2	1	1	2	3	3	2	1	1	2	3	3
O(1,2)	4e,4f	$2 \times C_{3v}^d$ (4)	2	0	0	2	2	2	2	0	0	2	2	2
O(3)	6h	C_{2v}'' (6)	1	1	1	0	1	2	0	1	1	1	2	1
O(4,5)	2 × 12k	$2 \times C_s^d$ (12)	4	2	2	4	6	6	4	2	2	4	6	6
Total			11	4	6	10	14	17	10	7[a]	4	12	18[a]	15

[a] For each of these symmetries, the total includes one acoustic mode (doubly degenerate for E_{1u}).

mid-IR segment, which was taken from a film of 6 μm, to match the main band, suggests that the far-IR spectrum was obtained from a film with $d = 1.5$ μm (Hofmeister et al., 2003). Fitting these results with a damped harmonic oscillator model reproduced the TO and LO positions obtained from analysis of single-crystal reflectance data (Jacobson and Nixon, 1968; Galtier et al., 1972).

Applying Eqn. 1 to the broad fringes in the mid-IR segment of corundum (Fig. 3d) gives 0.45 ± 0.5 μm as the spacing between the diamond anvils. This low value is assumed to represent the film thickness. Spectra calculated for the two orientations from the classical dispersion analysis of Barker (1967) have much sharper peaks than do the thin-film spectra (Fig. 3d). The $\mathbf{E} \perp \mathbf{c}$ polarization dominates the measured absorption spectrum, such that peaks from E ∥ c are present only as shoulders. With this orientational effect in mind, the discrepancy between the ideal and measured absorption coefficients is largest for the strong mid-IR bands, consistent with the discussion in Section 3.4. The absorption coefficient of the weakest peak of corundum at 385 cm^{-1} is well represented by the thin-film data, suggesting that A for the weak far-IR peaks of the calcium aluminates are well represented by the IR measurements.

For $CaAl_2O_4$ (Fig. 3a), the interference fringes suggest a distance of 1.75 μm for the thin mid-IR film, and 4.2 μm for the thicker film. These values clearly represent the gap between the diamonds rather than the film thickness because the peaks of the thick film are 3.80 times more intense than those of the thin film. If we assume that the same gap exists between the film and one diamond in both measurements, then the thinner of the mid-IR films for $CaAl_2O_4$ is below ~0.8 μm thickness.

Similarly, the upper limit is ~0.3 μm for the thinner mid-IR film of grossite, and the film-diamond gap is 1 μm. For synthetic hibonite, the thinner film has thickness below ~0.4 μm, for a film-diamond gap of 0.6 μm. The inferred air gaps are rather consistent, averaging 0.9 μm. From this we suggest that the thicker mid-IR segments in Figure 3 each have a thickness of 3.0 μm ($CaAl_2O_4$), 1.5 μm (grossite), and 2.2 μm (synthetic hibonite). All thicknesses are upper limits.

For hibonite (Fig. 3c), we observed 22 peaks out of the 23 possible for an unpolarized spectrum (Table 11b). Probably a singly-degenerate A_{2u} mode, rather than a doubly-degenerate E_{1u} mode, is masked. The broad band at 197 cm^{-1} may represent this hidden mode or could be a resonance of the acoustic and IR modes. For grossite (Table 12), 30 out of 33 expected, singly-degenerate, modes are seen. For $CaAl_2O_4$ (Table 13), only 48 of the expected 123 modes are detected. Observing half of the number of expected peaks suggests that not only do the two polarizations provide similar mode frequencies, but accidental degeneracies exist within each symmetry as well. The small fraction of modes observed may be consistent with the presence of strongly pseudoorthorhombic symmetry. The structure of monoclinic $CaAl_2O_4$ was refined in the space group $P2_1/n$ with $\beta = 90.2°$, and it is probable that the crystal studied was twinned by pseudo-merohedry.

The mid-IR peaks are not as well fit with Lorentzian shapes as are the far-IR peaks, because these contain a significant contribution of the LO modes. FWHM values in Tables 11b, 12, and 13 can be used to reconstitute the mid-IR spectra, but seriously overestimate the phonon-lifetimes, and are not used in computing thermal conductivity (Hofmeister, in press). The Raman modes do not have this problem as TO-LO splitting is not present, and thus the average FWHM of all Raman modes is compared to that of the far-IR modes (Tables 11–13).

For hibonite, <FWHM> is 10.0 cm^{-1} for the peaks below

Table 9. Symmetry analysis of grossite (C_{2h}^6 with Z = 2 in the primitive cell and 72 total vibrations).

Atom	Site	Symmetry	Raman A_g	Raman B_g	IR A_u	IR B_u
Ca	2e	C_2 (2)	1	2	1	2
Al(1,2)	2 × 4f	$2 \times C_1$ (4)	6	6	6	6
O(1)	2e	C_2 (2)	1	2	1	2
O(2,3,4)	3 × 4f	$3 \times C_1$ (4)	9	9	9	9
Total			17	19	17[a]	19[a]

[a] For these categories, one acoustic mode must be subtracted from A_u and B_u to obtain the correct number of IR active modes.

Table 10. Symmetry analysis of $CaAl_2O_4$ (C_{2h}^5 with Z = 12 and 252 total vibrations).

Atom	Site	Symmetry	Raman A_g	Raman B_g	IR A_u	IR B_u
All	21 × 4e	$21 \times C_1$ (4)	3	3	3	3
Total			63	63	63[a]	63[a]

[a] For these categories, one acoustic mode must be subtracted from A_u and B_u.

450 cm^{-1}, excluding the extremely broad and weak peak near 200 cm^{-1} that is probably an unresolved doublet (Table 11b). This is in excellent agreement with <FWHM> of 9.8 cm^{-1} obtained from the Raman data. The far-IR peaks provide 9.5 cm^{-1} for grossite, also in agreement with <FWHM> of 8.9 cm^{-1} for the Raman peaks. Far-IR peaks provide <FWHM> = 10.1 cm^{-1} for $CaAl_2O_4$, which is much less than <FWHM> of 14.3 cm^{-1} for the Raman peaks The far-IR value is used to represent $CaAl_2O_4$, assuming that unresolved doublets are present in the Raman spectrum of this phase.

5.2.2. Isotopic substitution in grossite

Grossite enriched with ~10% ^{17}O was produced by multiple grindings and sinterings and studied by nuclear magnetic resonance methods (Stebbins et al., 2001). The purity of these runs was checked using powder XRD. Infrared spectra of the doped and isotopically normal samples are similar (Fig. 3b). Although individual peak widths and positions differ slightly, possibly arising from orientational differences of the crystallites crushed to form the thin film, the average widths of the far-IR peaks are similar. Hibonite peaks appeared in ~1/3 of the spectra acquired of the ^{17}O-enriched samples. Given that XRD did not detect this impurity, we conclude that this contaminant occurs as a few percent of the isotopically enriched sample. The nuclear magnetic resonance results should not be affected at such low levels, particularly as not all aliquots of the grossite sample have hibonite contamination.

That the IR spectra of isotopically enriched and normal grossite are virtually identical is attributed to the low amounts of enrichment (estimated by Stebbins et al., 2001, as ~10%, since losses occur due to volatilization during synthesis). If partial substitution occurs on a site and if changing the cation mass does not substantially alter the frequency, then local modes would not be resolved. The bands should be broader to a degree depending on the solid solution. Neither effect is seen, confirming that the amount of ^{17}O substituting is low, probably ~5 to 10%.

5.2.3. Natural terrestrial hibonite

Mid-IR spectra of black and brown hibonite samples are similar (Fig. 3a). The main difference is that black hibonite has additional weak and sharp peaks near 600, 962, and 1096 cm^{-1} (which may represent impurities) and one additional intense and broad peak near 1050 cm^{-1}. Because far-IR data were not collected of brown hibonite, we compare the black and synthetic samples.

As observed for the Raman spectra, the IR peaks for natural hibonite are broader and shifted to lower frequencies by ~30 cm^{-1} compared to synthetic hibonite (Fig. 3c). Table 11b lists one possible correlation of the peaks. The range 200–400 cm^{-1} is especially problematic. Two-mode behavior (Chang and Mitra, 1968, Section 4) seems to be present as natural hibonite has peaks that are not seen in synthetic material. The effects of metamictization are discussed in Section 6.2.

From Eqn. 1 and the fringe spacing, the gap between the diamonds is 1.98 μm for brown hibonite film and 2.63 μm for black hibonite. As black hibonite is less absorbant (Fig. 3c), these distances mainly represent the diamond-diamond gap, and the film thicknesses for the brown hibonite is ~1 μm. True

Table 11a. Raman peak parameters for synthetic and natural hibonite.

Synthetic		Brown		Black	
ν	FWHM	ν	FWHM	ν	FWHM
				154.7[a]	22.4[a]
193.7	9.9				
209.4 p	9.9	~210		197.6	71.9
250.5 p	5.5	~274		265.2	72.1
274.0	18.1[b]				
331.9	12.1	323	52	322.9	65.0
		351.3 i	5.5	350 i	
399.4 p	11.6	374	24	361.1	37.0
				401.0	84.1
449.5	9.5	453.4	29	446.3	27.8
457.8	8.5				
489.1	8.5			471.8	37.3
529.5	8.6				
564.5	8.6	504.3	65	501.4	49.6
624.5	9.8	552	~15	537.7	28.7
640.4	8.7	568	~15	572.4	74.9
683.8	11.7				
741.0	19.0[b]	642.3	31	640.3	84.3
773.9	8.1				
795.8	8.5	718.2	214	697.6	80.7
837.3	15.8			743.5	79.2
872.9	13.4			803.9	79.3
910.0	8.6	865.2	102	871.3	61.1
<621>	<9.8>				

p = polarization response; i = likely impurity.
[a] This feature is near the upper or lower end of the frequency range, and its parameters are uncertain.
[b] Peak inferred to be an unresolved doublet, and omitted from the average.

film thickness is determined through comparison with the reflectivity data, as discussed below.

5.3. IR Reflectance Spectra of Black Hibonite

Our raw reflectivity spectra (Fig. 4) are similar to data obtained by Mutschke et al. (2002), accounting for some of their spectra being scaled. Additional shoulders are resolved in our spectra. For $E \parallel c$, our sample from Evisa is ~10% more reflective than theirs, but their sample from Antsirabé is about half as reflective as either. For $E \parallel c$, our samples are about half as reflective as Mutschke et al. (2002) observed for Antsirabé hibonite (data on Evisa were not obtained). Because the absolute reflectivity observed here for $E \parallel c$ is questionable, Kramers-Kronig analysis was not performed for this orientation.

For $E \perp c$, 14 peaks of the 17 expected are observed, which can be attributed to the bands being broad and overlapping. Probably two overlapping peaks are not resolved. For $E \parallel c$, 11 peaks are observed, whereas only 6 peaks are expected. This behavior is unusual. Correlating the peaks for the two polarizations suggests that the $E \parallel c$ spectrum is contaminated with the strongest peaks from $E \perp c$. Excluding these five intruders reduces the count to six peaks for $E \parallel c$. This phenomena is known as polarization mixing. Although misorientation of the sample with respect to the polarizer can induce such extra peaks, a sampling error is unlikely as this would require similar misorientations in both our work and that of Mutschke et al.

Table 11b. IR peak parameters for hibonite.

Synthetic			Brown			Black						
ν	FWHM	Absorb.	ν	FWHM	Absorb.	ν	FWHM	Absorb.	TO	LO	FWHM	f
~88	~5	~0.007				~75	~25	weak	~68	75[d]		
120.7	16.5	0.141				98.4	10.8	0.021	~110?[d]			
						116.5	27.8	0.087	116	130	19	3.2
						137.4	42.0	0.042		208?[d]		
197.4[c]	53.8[c]	0.051[c]				191.9	42.6	0.060	190	191	7	0.11
~230		shoulder				226.7	25.3	0.050	230?			weak
289.6	6.6	0.128				244.9	29.1	0.039	250?			weak
~312	~9	~0.005				271.5	29.5	0.063				
327.0	13.0	0.032				288.7	22.9	0.108	288	290	17	0.30
334.6	7.1	0.175				326.9	34.5	0.064	~327	348[d]		
353.3	5.1	0.096										
374.0	7.6	0.205				344.4	18.6	0.058	350			weak
395.6	12.6	0.279				386.5	60.3	0.314	382	404	30	2.36
404.5	17	0.259										
460.3	21.3	0.120				462.3	64.8	0.36	456	479	34	0.88
472.0	20.9	0.427										
530	20	0.208	535	149	0.31	536	92	0.45	524			weak
552	13	0.076										
599	30	0.40				576.0[b]	36[b]	0.26[b]	~576[d]			
621	31	0.26	602	84	0.29	603.4	28	0.19	584	638	48	2.69
643[b]	50[b]	0.35[b]	682	152	0.10	621	143	0.41	664	670	~15	0.12
708.0	58.6	0.481	707	65	0.15	701	104	0.34	695			0.05
741.9	17.6	0.160							~680[d]			
787.5	68.9	0.589	759	44	0.13	755	86	0.34	748	733	~20	0.41
829.2 f	76.6	0.467	776	156	0.37	823	180	0.65	716	924	~30	0.59
877.1 f	85.8	0.347	848	137	0.25				~800	~850[d]		
945.6 f	71.8	0.176	987 f	121	0.13	963 f	105	0.17				
						1043	53	0.19				
						1099 f	120	0.26				
<434>[a]	<11.8>[a]											

f = fringe or LO mode, not included in averages.

[a] Average ν for all peaks, average FWHM is for the 12 far-IR peaks ($ν < 500$ cm^{-1}), excluding the broadest.

[b] At this frequency and above, the parameters were obtained from fitting the mid-IR data. Absorbances were obtained from scaling the mid-IR to match the far-IR, and pertain to a thickness of ~1 μm for synthetic and black hibonite.

[c] Probably an unresolved doublet.

[d] These peaks are in the $\mathbf{E} \parallel \mathbf{c}$ polarization.

(2002). The extra peaks are unlikely to be due to two-mode behavior, as this origin is inconsistent with the observed large peak widths. We cannot discern whether the $\mathbf{E} \perp \mathbf{c}$ spectrum is affected, because the modes from $\mathbf{E} \parallel \mathbf{c}$ are very weak compared to those in $\mathbf{E} \perp \mathbf{c}$. Section 6.2 argues that the cause is metamictization. Regardless of the origin, the existence of polarization mixing for the $\mathbf{E} \parallel \mathbf{c}$ precludes quantitative analysis. However, the data confirm that the questionable lowest frequency peak seen in the absorption spectra does exist at 71 cm^{-1}.

Using $n = 1.8$ from the visible region in Fresnel's equation:

$$R = (n - 1)^2/(n + 1)^2, \qquad (7)$$

suggests that $\mathbf{E} \perp \mathbf{c}$ has a back reflection above 1000 cm^{-1}, because the measured values of R in this spectral region are double the expected value. We therefore performed our Kramers-Kronig analysis not only on the raw data, but also scaled R by ½, and analyzed this as well to determine the sensitivity of the analysis to the absolute value of R. Scaling R mainly lowers the intensities of the calculated functions (Fig. 4b,c). Peak positions and widths are little affected.

By comparing the absorption coefficient calculated from the Kramers-Kronig analysis to the measured absorbance of natural hibonite (Fig. 4c), we can deduce the symmetries of the modes present in the absorption spectra for synthetic hibonite through the correlation in Table 11b. Also, matching peak profiles in Figure 4c allows inference of film thickness for the absorption measurements. Some of the tallest peaks overshoot the measurements, which is expected as the films have tiny cracks that leak light. The absorption coefficient is lower than the absorbance at several places (e.g., near 300 cm^{-1}), due to the $\mathbf{E} \parallel \mathbf{c}$ peaks not being present in the **a-a** section. The peak near 120 cm^{-1} is most reliable as the $\mathbf{E} \parallel \mathbf{c}$ peaks are very weak at low frequency. Using A calculated from the raw reflectivity gives $d = 0.8$ μm, whereas A calculated by scaling R by ½ gives $d = 1.6$ μm. We conclude that the film thickness is 1 μm for the spectra for the thicker black and brown samples, which is consistent with rough estimates from fringe spacings. The thicker mid-IR film of synthetic hibonite is thus also ~1 μm thick (Fig. 3c).

6. IMPLICATIONS

6.1. Why Synthesis is Difficult

Typically, refractory calcium aluminates are produced by multiple cycles of sintering and grinding stoichiometric mix-

Table 12. Peak parameters for grossite.

Raman ν	FWHM	IR ν	FWHM	FWHM[c]	Absorb.[c]
		75	2	4	weak
		89	5.1	6	0.007
		114	17.2	11.4	0.0079
134 p	8.8	135.5	6.5	6.0	0.014
		160.1	30[b]	32[b]	0.0422
184.7 p	6.5	190.0	6.7	7.5	0.039
202.6	6.2				
209.9	8.3	207.2	10.4	9.5	0.041
220.4	5.3	229.7	17.6	14.8	0.035
251.8	6.5	255.5	7.6	8.6	0.026
268.1	5.8				
281.5	14.2	289.2	15	13.3	0.056
321.7 p	12.1	312.2	5.9	7.0	0.020
330.7	13.2	328.3	12.3	11	0.026
356.1	8.0	360.2	8.7	9.4	0.061
397.6	14.9	375.6	e	9.0	0.020
411.9	9.5	424.5	e	9.7	0.061
457.1	7.2	444.5	e	30.6[b]	0.046
		541.2	e	18.2	0.084
567.9	10.0	577.7	e	24.8	0.084
630	7	639.4[a]	17.0[a]		0.0765[a]
659.8 p	9.3	659.3	13.7		0.0663
686.1 p	9.5	681.8	39.6		0.0714
		700.1	41.0		0.0759
713.9 p	8.4				
		746.0	16		0.0960
755.6	7.5				
792.9 p	9.7	780.8	19.2		0.0219
806.5	7.4	813.3	70.0[b]		0.183
837.0	16.5[b]	835.8	28.5		0.0444
		845.6	12.3		0.0384
		871.6	41.0		0.0693
908.9	10.2				
		942[b]	117[b]		0.1476
942.4	7.1	943.7	14.7		0.00810
<493>	<8.9>	<458>	<17.1>[d]	<11>	

The bottom line gives average values for the 25 observed Raman modes and the 30 observed IR modes. "p" denotes polarized modes.

[a] Above $\nu = 500$ cm^{-1} the fit was made to the mid-IR spectrum. The mid-IR data were scaled down to match the spectrum of the thinner film used to acquire the far-IR data. The absorbance thus pertains to a thickness of 0.14 μm.

[b] Probably involves an LO mode or a doublet, widths not included in averages.

[c] This FWHM column and the absorbance in the far-IR are from ^{17}O doped grossite. Peak positions equal those of the isotopically normal sample within uncertainties.

[d] For $\nu < 400$ cm^{-1} of isotopically normal grossite, <FWHM> = 9.5 cm^{-1}.

[e] Spectral region omitted because peaks for corundum were present and obscure the grossite peaks.

tures of carbonate (which converts to lime during heating) and corundum. Although powder X-ray diffraction indicates that the run products are pure, scanning electron microscopy has shown that this approach yields significant amounts of impurities (Geiger et al., 1988). Similarly, we found that laser-heating mixtures of oxides also produced mixtures of phases. However, better results, i.e., masses of single crystals, were obtained from laser-heating mixtures of $CaAl_2O_4$ and corundum.

Multiple phases exist in charges with hibonite stoichiometry because hibonite melts incongruently. However, additional phases are also found in runs intended to produce grossite, even

Table 13. Peak parameters for $CaAl_2O_4$.

Raman		IR		
ν	FWHM	ν	FWHM	Intensity
		67.9	4.9	0.073
		74.4	6.3	0.065
		113.1	7.0	0.149
		125.2	4.0	0.089
		130.5	4.1	0.110
140.3[d]	10.7[d]	136.6	4.5	0.067
148.7	8.7	147.5	6.5	0.187
		154.1	8.5	0.15
174.7	14.1	170.4	10.3	0.225
		185.8	19.8	0.299
202.9[e]	24.2			
		215.7	6.3	0.152
		221.3	9.7	0.25
		231.2	12.3	0.291
		241.6	14.7	0.199
249.3	12.8	249.2	11.5	0.149
		259.4	8.5	0.196
		268.7	9.0	0.124
277.7 p	18.5	278.7	18.2	0.094
		294.3	11.0	0.213
308.5	16.1	305.7	7.9	0.114
338.7	11.4	332	18	0.126
		350.7	12.4	0.195
		363.9	8.2	0.161
370	19.4	377.6	11.2	0.186
403.9	7.6	391.6	9.1	0.295
		417.8	11.6	0.513
		426.2	13.9	0.588
		434.2	11.9	0.394
440.9	12.7	448.6	11.4	0.381
		457.2	18.6	0.380
470.8	12.5	468.6	19.3	0.302
481.5	14.4			
519.1	15.7			
		530.9	8.9	0.08
543.6	14.9	543.7	13.4	0.14
562.8	24.7	575.1	22.9	0.33
615.8	17.0	b	b	b
645.8 p	20.5	640.9	11.5	0.437
658.5 p	12.0	655.3	19.8	0.437
		678.7	18.8	0.312
685.9	15.6	689.2	19.2	0.375
		700.4	19.5	0.306
718.9	10.2	726.7	12.6	0.344
		765.4	6.3	0.188
773.0	11.8			
786.7	19.5	782.4	19.9	0.813
		791.8	7.4	0.313
		803.9	12.9	0.781
808.7	5.9	810.2	7.9	0.297
		821.0	14.1	0.641
840.3	6.0	841.3	36.9	1.094
		869.1	14.3	0.278
879.4	34.9[c]			
<502>[a]	<14.3>[a]	<429>[a]	<12.4>[e]	

[a] Average values for the 26 observed Raman modes and the 48 observed IR modes. "p" denotes polarized modes.

[b] Above v = 600 cm^{-1} the fit was made to the mid-IR spectrum. The mid-IR data were scaled to match the spectrum of the thicker far-IR film The absorbance thus pertains to 3 μm thickness.

[c] This peak is probably a doublet, as its width is considerably larger than that of any other Raman peak, and is excluded from the average.

[d] Parameters uncertain because this peak is near the upper or lower end of the frequency range.

[e] For the far-IR region ($\nu < 450$ cm^{-1}) only, <FWHM> = 10 cm^{-1}, see text.

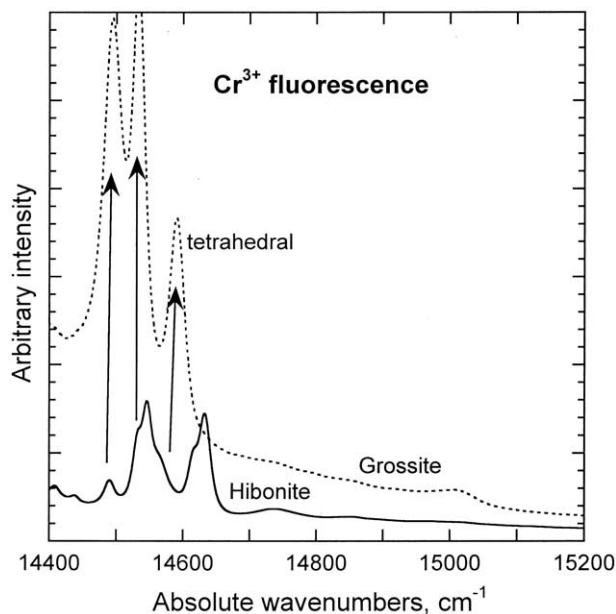Fig. 2. Photoluminescence spectra of Cr^{3+} ions in the synthetic hibonite and grossite. No peaks were seen in $CaAl_2O_4$, and thus the contaminant is in the Al_2O_3 starting material. Absolute wavenumber units are shown. Arrows connect peaks in grossite (which has only tetrahedral coordination) to similar peaks in hibonite (which has both tetrahedral and octahedral sites).

Fig. 1. Raman spectra of lattice modes. (a) End-member calcium aluminates. Peaks responding to polarization are indicated by an asterisk. The grossite spectrum was scaled by $\times 10$. Spectra are offset vertically for clarity. (b) Comparison of synthetic and natural hibonite. Arrows show plausible connections between peaks of the brown and synthetic samples.

though it melts congruently. Possibly, calcium aluminates are difficult to synthesize because the simple oxides are very stable. Using $CaAl_2O_4$ as a starting material provides juxtaposition of Ca and Al in a structure, and less drastic structural rearrangements are needed to incorporate additional Al and O ions to produce grossite and hibonite. Calcium aluminate also melts at a much lower temperature (a phase diagram is provided by Geiger et al., 1988). Quick cooling during laser heating pro-

vides many nuclei and rapid growth of small crystals. Better results (larger crystals and masses) should be obtained with homogeneous starting material of precisely the desired composition. Holding the fine-grained crystals at a temperature below, but close to, the solidus is also likely to yield bigger single-crystals, as was found in one attempt.

6.2. Metamictization of Terrestrial Hibonite

Damage by α-particles from U or Th decay causes a high density of point defects and dislocations (Murakami et al., 1991), which have been associated with spectral changes. Raman peaks of partially metamict zircons are broader and shifted to lower wavenumbers, due to increased irregularities in the bond lengths and angles and expansion of the lattice, respectively (Nasdala et al., 1995; Wopenka et al., 1996). In contrast, IR spectra of zircons have peaks that become weaker and broader as the degree of metamictization increases, but large shifts in position are not seen (Woodhead et al., 1991). IR anisotropy is partially destroyed by partial metamictization, and strongly metamict samples are isotropic (Woodhead et al., 1991).

Vibrational spectra of terrestrial Th-bearing hibonite show the combined effects of chemical substitution and radiation damage. The limited excitation volumes (due to dark sample colors) and the steep spectral backgrounds (due to laser-induced photoluminescence of trace elements) lead to weak Raman peaks. The downward shifts of ~ 30 cm^{-1} for many peaks in both Raman and IR spectra are due, at least partially, to substitution of heavier cations. Vibrational peaks also broaden due to cation disorder that accompanies chemical substitution.
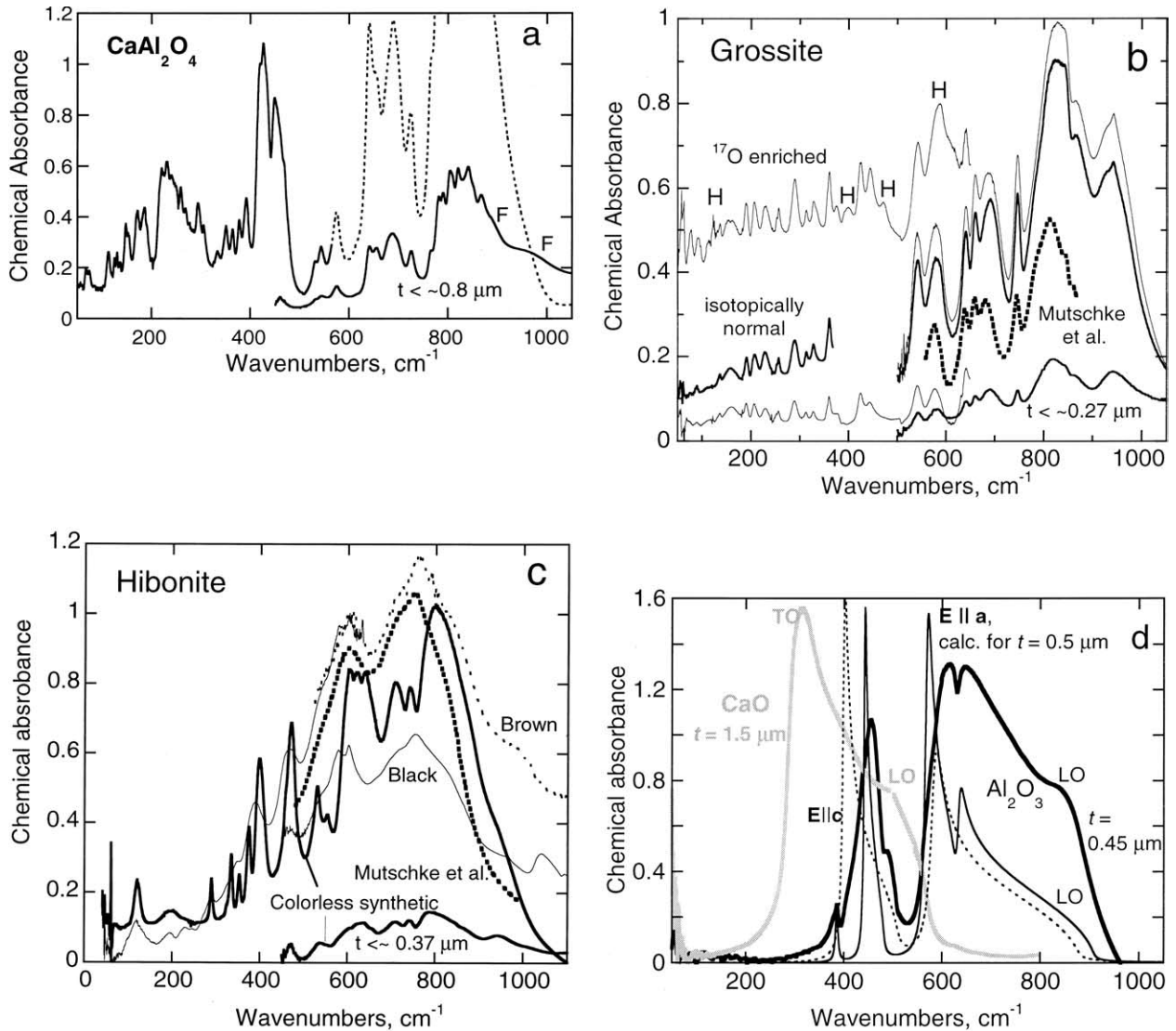
Fig. 3. IR spectra of thin films. F = interference fringe. See text for discussion of thickness. (a) CaAl$_2$O$_4$. Three different measurements are shown. (b) Grossite. Thin solid curves = enriched with ~10% ^{17}O (Stebbins et al., 2001). Thick solid curves = isotopically normal grossite (predominantly ^{16}O). Heavy dotted curve = grossite dispersed in KBr (Mutschke et al., 2002). H = peaks due to hibonite contamination. For isotopically normal grossite, the far-IR spectrum above 360 cm^{-1} is not shown because this range is contaminated by corundum impurities. (c) Hibonite. Thick solid line = synthetic. Thin solid line = black sample. Finely dotted curve = brown hibonite. Heavy dotted curve = natural hibonite dispersed in KBr (Mutschke et al., 2002). (d) Lime (gray lines) from Hofmeister et al. (2003) and corundum (various black lines). Thick solid curve = thin films. Thin solid curve = ideal absorption calculated for $\mathbf{E} \perp \mathbf{c}$ from classical dispersion analysis of reflectivity data of Barker (1967). Dotted = calculation for $\mathbf{E} \parallel \mathbf{c}$.

The increase in IR band widths upon chemical substitution is less than the increase in Raman widths because IR absorption peaks are inherently broad as these contain both the TO and LO modes (Wooten, 1972). Raman peaks should represent only one mode for most mineral structures. Both the broadening of the peaks and the large shifts are excessive given the degree of chemical substitution in Madagascar hibonite. Furthermore, the IR modes of hibonite do not follow the divisions into different polarizations required by symmetry analysis. Because IR vibrations are active when the dipole associated with the atomic motions is perpendicular to the direction of propagation of the IR beam, the large degree of polarization mixing observed

implies that the damage to the unit cell shifts or rotates the atoms from their expected positions, and thus the orientation of the dipoles changes, and the symmetry of the IR bands is altered. Our measurements are not sufficient to detect whether the expected polarizations are violated by the Raman-active modes, but are consistent with the observations of Woodhead et al. (1991).

Inference of radiation damage is supported by the results of Holstam (1996), who found that Mössbauer spectra of natural (Madagascar) hibonite with ~0.7 wt.% Th are less distinct than those of synthetic hibonite with similar Fe and Ti contents. The high Th content and the considerable age of the locality (515 to
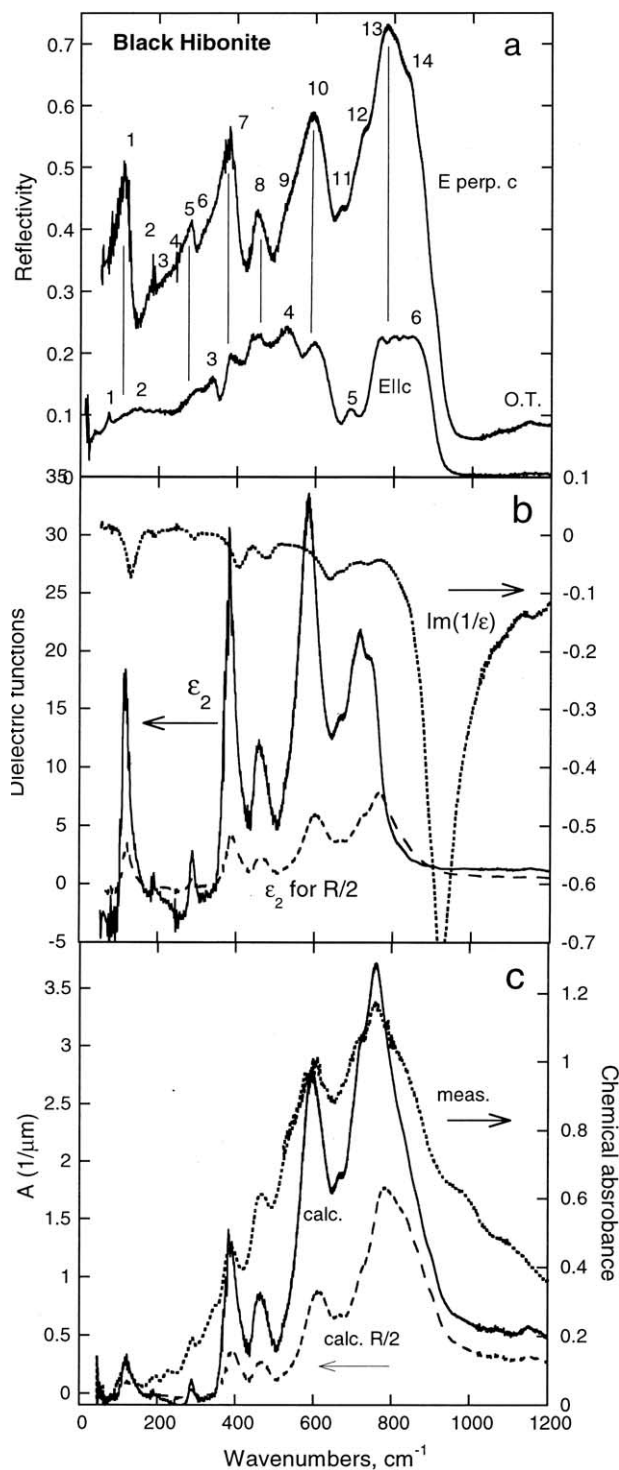
Fig. 4. IR reflectance data and functions derived from Kramers-Kronig analysis of black hibonite. (a) Reflectivity. Upper curve, $\mathbf{E} \perp \mathbf{c}$. Lower curve, $\mathbf{E} \parallel \mathbf{c}$. The fundamentals intrinsic to each polarization are consecutively numbered. Vertical lines indicate which peaks in $\mathbf{E} \parallel \mathbf{c}$ are artifacts from polarization mixing. O.T. = overtone-combination. (b) The dielectric functions ε_2 (solid line, left scale) and $im(1/\varepsilon)$ (broken line, right scale). The effect of dividing R by 2 on ε_2 is shown as a dashed line. (c) Comparison of calculated absorptivity for $\mathbf{E} \perp \mathbf{c}$ (solid line) with measured absorbance (dotted line). Dashed line = the effect of dividing R by 2 on the calculation of A.

564 Ma: Moine et al., 1997; Pezzota and Simmons, 2001) points to radiation damage being present in hibonite from Madagascar. Our structure refinements for both synthetic and brown hibonite are of similarly high quality, suggesting that the radiation damage can be only partial.

Because of the structural damage and spectral changes associated with metamictization, IR spectra of Madagascar hibonite are not appropriate for comparison with astronomical environments. For experiments where the structure plays a role, terrestrial Th-bearing hibonite may not be a good analog for meteoritic samples.

6.3. Evidence for Hibonite and Grossite in Proto-planetary Nebula

6.3.1. Astronomical data examined here

The bright and bipolar planetary nebula NGC 6302 with its very hot central star is of interest as these characteristics suggest a massive progenitor. Analysis of the complete Infrared Space Observatory (ISO) spectrum indicates the presence of essentially end-member forsterite and enstatite (Molster et al., 2001). The dust shell around another evolved star produces virtually the same spectrum (NGC 6537, see Kemper et al., 2002). Kemper et al. (2002) found evidence for diopside and suggested that calcite and dolomite [$CaMg(CO_3)_2$] are present. However, not all of the sharp peaks have been identified in either of these studies, and carbonates are not expected to occur in such environments (Lodders and Fegley, 1999; Lodders, 2003).

6.3.2. Conditions in the Nebula NGC 6302 and criteria ssed to identify its mineral species

This object is in emission. As discussed in Section 3.4.3, the spectrum of the nebula is the product of Planck's function and the absorption data. To understand how complex the situation is, we consider how grains of different sizes and temperatures would contribute to the IR spectrum of the nebula, using synthetic hibonite as an example (Fig. 5). Large grains are opaque and emit as blackbodies. As grain size decreases, the peaks are better resolved, until the material is so fine that little light is provided. Grain sizes producing recognizable spectra are compatible with those seen in primitive meteorites. Uncertainties in our thicknesses are immaterial given the ranges of grain size and of temperature, and the number of phases needed to model the nebula, as follows.

The spectrum of the nebula is dominated by that of a blackbody at 47 K. However, considerable intensity exists above ~ 300 cm^{-1} indicating that a substantial fraction of the dust is at higher temperatures. No single temperature describes the nebula. Most of the material falls in the range $\sim$!30 to 80 K (Fig. 5), but higher and lower cryogenic temperatures are possible for a fraction of the dust. Neither could the nebula be fit with a unique temperature distribution.

That the dust grains have cryogenic temperatures is important. The tail of Planck's curve cuts off the high-frequency modes (Fig. 5), leading to the loss of a spectral pattern for any given mineral above some certain frequency. This cutoff frequency will depend on the grain size, as shown for hibonite in Figure 5. As a corollary, the cutoff frequency must also depend
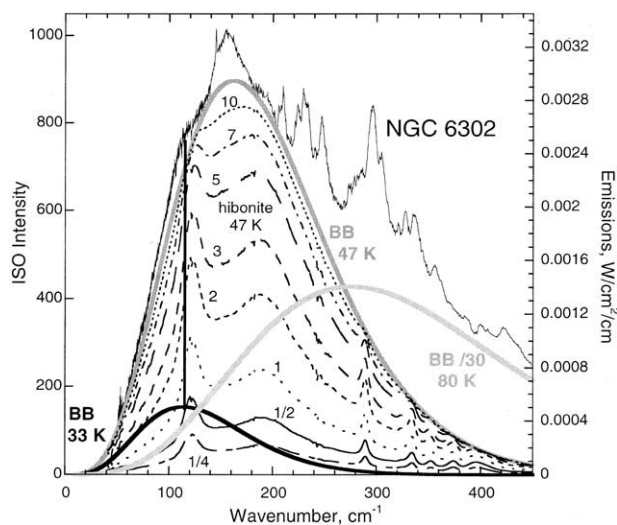
Fig. 5. Comparison of emission spectra of blackbodies and of synthetic hibonite to a proto-planetary nebula. A blackbody curve (gray line, right Y-scale) for 47 K fits the low-frequency slope and has its maximum at the same position as the nebula's emission spectrum. The blackbody curve for 33 K (heavy black line) has a maximum where the nebula spectrum has a strong shoulder. The blackbody curve for 80 K (thick light-gray curve) was divided by 30 to plot on the same scale and to show the match with the trend in the nebula's spectrum at high ν. Thin and patterned lines are emission spectra for synthetic hibonite, with thickness in μm as labeled. Laboratory data are for room temperature, and therefore the peaks are broader than would be encountered at 47 K.

on the intensity of the modes involved. Because the intensity of the modes tends to increase with frequency (next section), each mineral will have a cutoff frequency corresponding to the division of the spectrum into weak and strong modes. This behavior is clearly seen for silicates (see below).

From Figure 5, it is clear that no unique grain size will fit the data and that a blackbody contribution summed with emission spectra appropriate for small mineral grains describes the nebula. However, the composition of the material contributing to the blackbody curve cannot be ascertained. It could be carbon, metallic iron, or large mineral grains, or clumps of tiny grains. Thus, the bulk chemical composition of the dust in the nebula cannot be ascertained by any fitting procedure. Only the constitution of small, isolated grains can be determined.

Given the above problems, this study simply uses pattern recognition to identify the mineral species present in NGC 6302. Because the dust in space is cold, the peaks will be narrower than in the room temperature measurements, due to depopulation of vibrational states, and will be shifted to higher frequency, due to contraction of the lattice. However, the observed shifts of various silicates (Bowey et al., 2001) are small, $<\sim 2$ cm^{-1}. We assume that the calcium aluminates will behave similarly, and use peak position, shape, and relative intensity, but not width, in ascertaining the presence of a species (except for silicates, where some data on widths are available). Thin-film spectra are used, and calculated A, where available, to provide emissivity close to the intrinsic values (see Section 3.4; Hofmeister et al., 2000, 2003).

6.3.3. The mineralogy of dust in NGC 6302

The spectral patterns of forsterite and pyroxenes (Fig. 6a) are clearly recognized in NGC 6302 as shown earlier (Molster et al., 2001; Kemper et al., 2002). Forsterite peaks near 140 and 200 cm^{-1} are considerably narrower in the nebula than in the laboratory measurements, whereas the cluster near 300 cm^{-1} provides a better match. This behavior is consistent with cryogenic laboratory measurements of Mg_2SiO_4 (Bowey et al., 2001). In contrast, widths for the pyroxene peaks did not decrease upon cooling (Bowey et al., 2001). These pyroxene samples have Fe ($\sim$10% substitution for Mg in enstatite, and $\sim$3% in diopside), which may inhibit peak narrowing, as olivine peaks did not sharpen as much as did those of forsterite upon cooling. The nebula has peaks at positions indicative of enstatite and diopside, but with narrower widths than the laboratory spectra, and this may be due to the pyroxenes in the nebula being essentially Mg end-members. Another concern is that the diopside spectrum does not quite match the nebula peak at 160 cm^{-1}.

Calcium aluminates (Fig. 6b) match the peaks not covered by the silicates, in particular, the regions near 100 and 210 cm^{-1}, and above 320 cm^{-1}. The weak peak in the nebula near 305 cm^{-1} is very close to the only weak peak in spinel ($MgAl_2O_4$). Similarly, evidence for the two weak peaks at 385 and 400 cm^{-1} in corundum is seen. All the peaks observed below 440 cm^{-1} in grossite, spinel, and corundum are seen in the nebula spectrum. The far-IR intensities for these materials are all weak, and their higher frequency peaks are very strong. Hibonite behaves like forsterite and the pyroxenes, in that all its peaks observed below 360 cm^{-1} are seen in the nebula spectrum, but the intense peaks at higher frequency are not.

Melilite-group minerals (Fig. 6c) were investigated because of their association with hibonite in CAIs. These phases have intense bands above 270 cm^{-1}, which are not seen in the nebula spectrum. All their low-frequency, weak bands are present. Gehlenite ($CaAl_2SiO_7$) provides an excellent match for all of the low-frequency peaks except those associated with forsterite, although the maximum of the nebula is not fit well unless an akermanite component ($Ca_2MgSi_2O_7$) is present (Fig. 6c). Melilite-group minerals have peak positions similar to those of pyroxenes, owing to structural similarities. The match for gehlenite appears to be better than the match for enstatite and diopside together. For all of these silicates, the fit to the nebula peak at 160 cm^{-1} is less than ideal, but grossite contributes to this region as well.

Peaks in the nebula are assigned to mineral phases in Figure 7. Peaks above 300 cm^{-1} in the nebula spectrum correlate with a single mineral, whereas peaks at low ν correlated with two (and sometimes more) minerals. The region near 230 cm^{-1} is oversubscribed by mineral phases, as well as by the possible presence of ice. For each mineral, all peaks below a certain frequency are present in the nebula.

Based on the uniqueness of the spectral matches, the following minerals are unequivocally present in NGC 6302: forsterite and grossite (Figs. 6 and 7). The identification of hibonite is robust (but not unequivocal) due to the number of bands, the frequency range, and the band shapes. The presence of corundum has an extremely high degree of certainty due to spectral matches and to known mineral associations in CAIs. The pres-
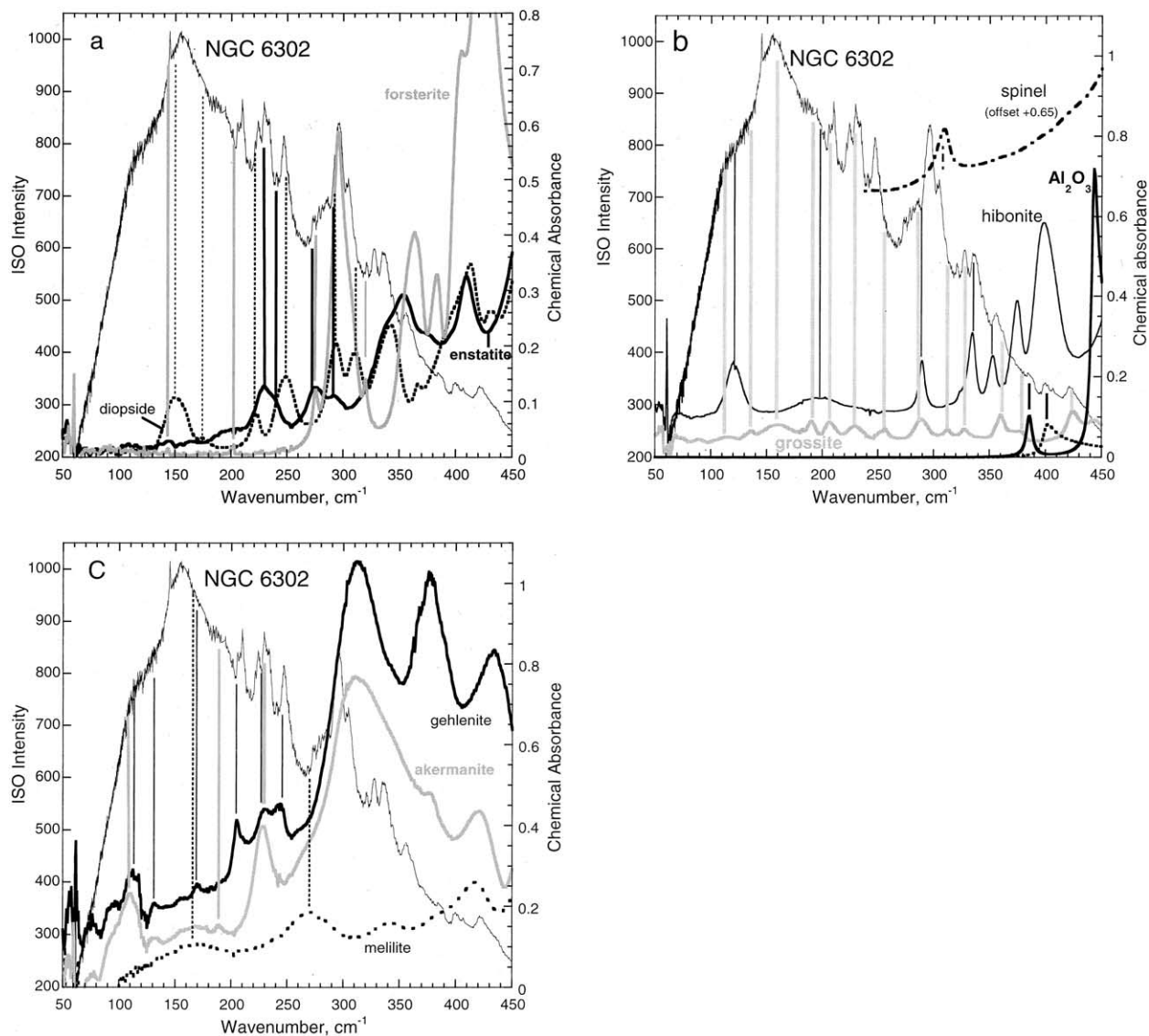
Fig. 6. Comparison of far-IR absorption spectra from thin films with emission spectra from a proto-planetary nebula (NGC 6302). The astronomical data (light solid lines, left scale) are presented by Molster et al. (2001) and Kemper et al. (2002) and were provided by T. Lim and J. E. Bowey. As the nebula is cold, the peaks above ~300 cm^{-1} are weakly excited, and the intensities will be much less than in our room-temperature absorption spectra (see text). Chemical absorbance is plotted on the right scale for various minerals. For each mineral, vertical patterned lines connect its peaks with those of the nebula. Asterisks indicate peaks unaccounted for by each mineral grouping. (a) Silicates. Samples are described in Section 2.3. Gray curve = forsterite. Thick black = enstatite. Dotted = diopside. No silicate features can be matched above 320 cm^{-1}, even if widths and intensity variations are accounted for. (b) Calcium aluminates and oxides. CaO or CaAl$_2$O$_4$ features do not correlate with those of the nebula, and are not shown. All of the grossite (gray curve) peaks below 450 cm^{-1} match. All of the hibonite (thin black curve) peaks below 360 cm^{-1} match. All of the weak far-IR peaks of corundum (thick curves at bottom) and MgAl$_2$O$_4$ (dot-dashed curve, data from Chopelas and Hofmeister, 1991) are seen. (c) Melilite group. Peaks due to gehlenite dominate the nebula spectrum below 250 cm^{-1}, but the matches are less than satisfactory. Noise is due to the rotational bands of H$_2$O not removed by evacuation.

ence of diopside, enstatite, and gehlenite are highly likely due to spectral matches, but overlaps make it difficult to ascertain which phase is present, or if all phases are present, and questions exist as to the widths of the pyroxene peaks. It is also possible that akermanite or a solid solution melilite are present. Spinel is probably present, as no other matches were found for the 305 cm^{-1} peak.

Calcite has previously been identified on the basis of its

~110 cm^{-1} peak (Kemper et al., 2002). However, this nebular feature correlates with hibonite and grossite, or with akermanite, or gehlenite, and their higher frequency peaks match as well. Because the band near 110 cm^{-1} (a translation of Ca) is common to silicates, alumino-silicates, and carbonates, it alone cannot be used to ascertain a specific mineral. Similarly, the 160 cm^{-1} peak from the nebula need not be due to dolomite, as it matches peaks from grossite, diopside, akermanite, or me-
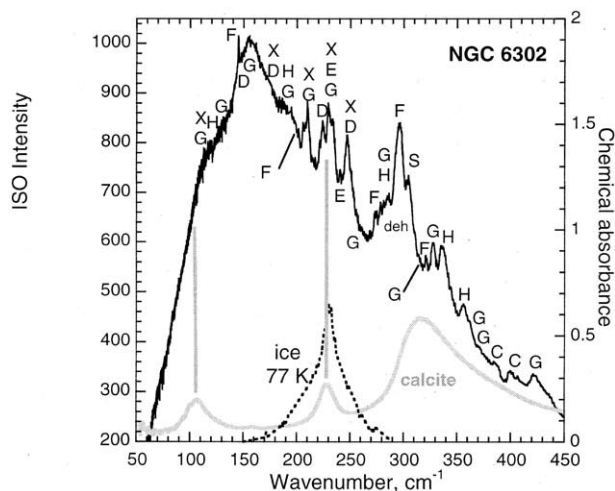
Fig. 7. Assignment of peaks in the nebula spectrum (black curve) to minerals. C = corundum; D = diopside; E = enstatite; F = forsterite; G = grossite; H = hibonite; S = spinel; X = gehlenite. The symbol "deh" indicates that several peaks from diopside, enstatite, and hibonite could underlie the complex at 300 cm^{-1}. Gray line = absorption spectrum of calcite. Dotted line = absorption spectrum of water ice at 77 K. Several silicates or oxides match the peaks that might be traceable to calcite.

lilite. The presence of calcite is very unlikely, as it is not part of the condensation sequence for a nebula with a solar-type composition (Lodders, 2003). Inconsistencies with data on meteorites are discussed by Kemper et al. (2002).

7. CONCLUSIONS

Interpretation of observed astronomical spectra is made through comparison with laboratory measurements. The correctness of an interpretation is predicated on the observational and laboratory data being collected under similar conditions, including temperature. Data on a wide variety of candidate minerals is helpful. Our thin-film IR spectra of synthetic calcium aluminates represent the end-member or near-end-member compositions likely to be found in astronomical environments. Comparison of thin-film absorption spectra to absorption coefficients extracted from reflectivity of natural hibonite supports the quantitative nature of thin-film spectra. Terrestrial hibonite, however, should not be used to evaluate astronomical data, because of radiation damage and significant cation substitutions.

The match of a spectral pattern is needed to unequivocally identify minerals in space. Obviously, the more peaks that are involved in the match, the more certain the assignment. Because all 13 grossite peaks below 450 cm^{-1} correlate with features in the spectrum of NGC 6302, its presence is undeniable. Because all five hibonite peaks below 360 cm^{-1} correlate with features in the spectrum of NGC 6302, and because no other phase matches some of these peaks, its presence is relatively certain. Forsterite is the only other mineral clearly present in the nebula (five of its peaks match). Matches for corundum and spinel are unique, but not robust, as few peaks are involved. Pyroxenes or melilites, or both, are also present.

To determine the proportions of the phases in the small grain fraction, the nebula spectrum should be fit by a combination of the various mineral spectra. For a more robust fit, low-temperature data are needed. Data on sodic gehlenite are needed as well, and other refractory phases might be considered. However, the large number of variables involved (>7 minerals, each with a range of temperatures and grain sizes) means that fitting the nebula is underconstrained.

The nebular mineralogy determined on the basis of pattern recognition is significant for two reasons. First, it recapitulates the condensation sequence. All of the oxide phases in Table 7 of Lodders (2003) were identified, with the exceptions of those containing Ti and anorthite. Because of the low abundance of Ti, such phases would be difficult to detect. Anorthite may not be present if Ca or Al were consumed by condensation of phases forming earlier in the sequence. This phase should be considered in future fits for thoroughness. Second, the deduced mineralogy includes the presolar phase hibonite, and probably corundum and spinel. Previous identifications of these minerals have been debated.

REFERENCES

Andermann G., Caron A., and Dows D. A. (1965) Kramers-Kronig dispersion analysis of infrared reflectance bands. *J. Opt. Soc. Am.* **55,** 1210–1216.

Armstrong J. T. (1988) Bence-Albee after 20 years: Review of the accuracy of a-factor correction procedures for oxide and silicate minerals. In *Microbeam Analysis* (ed. D. E. Newbury), San Francisco Press, Inc., pp. 469-476.

Barker A. S. (1967) Infrared lattice vibrations and dielectric dispersion in corundum. *Phys. Rev.* **132,** 1474–1481.

Bermanec V., Holtstam D., Sturman D., Criddle A. J., Back M. E., and Šcavnicar S. (1996) Nežilovite, a new member of the magneto-plumbite group, and the crystal chemistry of magnetoplumbite and hibonite. *Can. Mineral.* **34,** 1287–1298.

Bischoff A., Keil K., and Stöffler D. (1985) Perovskite-Hibonite-Spinel-bearing inclusions and Al-rich chondrules and fragments in Enstatite chondrites. *Chem. der Erde* **44,** 97–106.

Bowey J. E., Lee C., Tucker C., Hofmeister A. M., Ade P. A. R., and Barlow M. J. (2001) Temperature effects on the 15–85 μm spectra of olivines and pyroxenes. *Mon. Not. Roy. Astr. Soc.* **325,** 886–896.

Brearley A. J. and Jones R. H. (1998) Chondritic meteorites. *Rev. Miner.* **36,** 3-1–3-398.

Brewster M. Q. (1992) *Thermal Radiative Transfer and Properties.* John Wiley and Sons, Inc., New York, pp. 229–230, 374–382, 385–386, 424–426.

Bruker-AXS (1998a) *SAINT, V 5.01 program for reduction of data collected on Bruker AXS CCD area detector systems.* Bruker Analytical X-ray Systems, Madison, Wisconsin.

Bruker-AXS (1998b) *XPREP V5.0 program for Data Preparation and Reciprocal Space Exploration.* Bruker Analytical X-ray Systems, Madison, Wisconsin.

Bruker-AXS (1998c) *SHELXTL NT, V5.1 program suite for solution and refinement of crystal structures.* Bruker Analytical X-ray Systems, Madison, Wisconsin.

Burns G. (1990) *Solid State Physics.* Academic Press, San Diego.

Burruss R. C., Ging T. C., Eppinger R. G., and Samson I. M. (1992) Laser-excited fluorescence of rare earth elements in fluorite: Initial observations with a laser Raman microprobe. *Geochim. Cosmochim. Acta* **56**, 2713–2723.

Chang I. F. and Mitra S. S. (1968) Application of a modified long-range iso-displacement model to long-wavelength optic phonons of mixed crystals. *Phys. Rev.* **172**, 924–933.

Charlu T. V., Newton R. C., and Kleppa O. J. (1981) Thermochemistry of synthetic $Ca_2Al_2SiO_7$ (gehlenite)-Ca_2MgSi_2O (akermanite) melilites. *Geochim. Cosmochim. Acta* **45**, 1609–1617.

Choi B., Wasserburg G. J., and Huss G. R. (1999) Circumstellar hibonite and corundum and nucleosynthesis in asymptotic giant branch stars. *Astrophys. J. Lett.* **522**, L133–L136.

Chopelas A. and Hofmeister A. M. (1991) Vibrational spectroscopy of aluminate spinels at 1 atm and of MgAl2O4 to over 200 kbar. *Phys. Chem. Miner.* **18**, 279–293.

Christophe Michel-Lévy M., Kurat G., and Brandstätter F. (1982) A new calcium-aluminate from a refractory inclusion in the Leoville carbonaceous chondrite. *Earth Planet. Sci. Lett.* **61**, 13–22.

Curien H., Guillemin C., Orcel J., and Sternberg M. (1956) La hibonite, nouvelle espèce minérale. *C. R. Hebd. Séances Acad. Sci.* **242**, 2845–2847.

Deer W. A., Howie R. A., and Zussman J. (1978) *Rock-Forming Minerals.* Halstead Press, London.

Dougill M. W. (1957) Crystal structure of calcium monoaluminate. *Nature* **180**, 292–293.

Drake M. J., and Weill D. F. (1972) New rare earth element standards for electron microprobe analysis. *Chem. Geol.* **10**, 179–181.

Farmer V. C. and Lazarev A. N. (1974) Symmetry and crystal vibrations. In *The Infrared Spectra of Minerals* (ed. V. C. Farmer), pp. 51–68. Mineralogical Society, London.

Fateley W. G., Dollish F. R., McDevitt N. T., and Bentley F. F. (1972) *Infrared and Raman Selection Rules for Molecular and Lattice Vibrations: The Correlation Method.* Wiley Interscience, New York.

Floss C., El Goresy A., Zinner E., Palme H., Weckwerth G., and Rammensee W. (1998) Corundum-bearing residues produced through the evaporation of natural and synthetic hibonite. *Meteorit. Planet. Sci.* **33**, 191–206.

Gaines R. V., Skinner H. C. W., Foord E. E., Mason B., and Rosenzweig A. (1997) *Dana's New Mineralogy.* John Wiley and Sons, New York.

Galtier M., Montaner A., and Vidal G. (1972) Phonons optiques de CaO, SrO, BaO au centre de la zone de Brillouin à 300 et 17K. *J. Phys. Chem. Solids* **33**, 2295–2302.

Geiger C. A., Kleppa O. J., Mysen B. O., Lattimer J. M., and Grossman L. (1988) Enthalpies of formation of $CaAl_4O_7$ and $CaAl_{12}O_{19}$ (hibonite) by high temperature, alkali borate solution calorimetry. *Geochim. Cosmochim. Acta* **52**, 1729–1736.

Goodwin D. W. and Lindop A. J. (1970) The crystal structure of $CaO.2Al_2O_3$. *Acta Cryst.* B26, 1230–1235.

Greshake A., Bischoff A., Putnis A., and Palme H. (1996) Corundum, rutile, periclase, and CaO in Ca, Al-rich inclusions from carbonaceous chondrites. *Science* **272**, 1316–1318.

Grossman L. (1980) Refractory inclusions in the Allende Meteorite. *Ann. Rev. Earth Planet. Sci.* **8**, 559–608.

Hawthorne F. C., Ungaretti L., and Oberta R. (1995) Site populations in minerals: Terminology and presentation of results of crystal structure refinement. *Can. Mineral.* **33**, 907–911.

Hoerkner W. and Mueller-Buschbaum H. (1976) Zur Kristallstruktur von $CaAl_2O_4$. *J. Inorgan. Nuclear Chem.* **38**, 983–984.

Hofmeister A. M. (1995) Infrared microscopy in the earth sciences. In *Practical Guide to Infrared Microspectroscopy* (ed. H. Humicki), pp. 377–416. Marcel Dekker Inc., New York.

Hofmeister A. M. (in press) Physical properties of the CaO-Al_2O_3 system from vibrational spectroscopy. *Geochim Cosmochim Acta.*

Hofmeister A. M. and Mao H. K. (2001) Evaluation of shear moduli and other properties of silicates with the spinel structure from IR spectroscopy. *Am. Miner.* **86**, 622–639.

Hofmeister A. M., Keppel E., Bowey J. E., and Speck A. K. (2000) Causes of artifacts in the infrared spectra of powders. In *ISO Beyond the Peaks: The 2nd ISO Workshop on Analytical Spectroscopy* (eds. A. Salama, M. F. Kessler, K. Leech, and B. Schulz), pp. 343-346, European Space Agency, Madrid, Spain.

Hofmeister A. M., Keppel E., and Speck A. K. (2003) Absorption and reflection IR spectra of MgO and other diatomic compounds. *Mon. Not. R. Astron. Soc.* **345**, 16–38.

Hofmeister A. M., Giesting P. A., Wopenka B., Gwanmesia G. D., and Jolliff B. L. (2004) Vibrational spectroscopy of pyrope-majorite garnets: Structure and order. *Am. Miner.* **89**, 132–146.

Holtstam D. (1996) Iron in hibonite: A spectroscopic study. *Phys. Chem. Minerals.* **23**, 452–460.

Huss G. R., Fahey A. J., Gallino R., and Wasserburg G. J. (1994) Oxygen isotopes in circumstellar Al_2O_3 grains from meteorites and stellar nucleosynthesis. *Astrophys. J.* **430**, L81–L84.

Ibers J. A. and Hamilton W. C. (1974) *International Tables for X-ray Crystallography, IV.* The Kynoch Press, Birmingham, U.K.

Ivanova M. A., Petaev M. I., MacPherson G. J., Nazarov M. A., Taylor L. A., and Wood J. A. (2002) The first known natural occurrence of calcium monoaluminate, in a calcium-aluminum-rich inclusion from the CH chondrite Northwest Africa 470. *Meteor. Planet. Sci.* **37**, 1337–1344.

Jacobson J. L. and Nixon E. R. (1968) Infrared dielectric response and lattice vibrations of calcium and strontium oxides. *J. Phys. Chem. Solids* **29**, 967–976.

Jarosewich E. and Boatner L. A. (1991) Rare-earth element reference samples for electron microprobe analysis. *Geostandards Newsletter* **15**, 397–399.

Kato K. and Saalfeld H. (1968) Verfeinerung der Kristallstruktur von CaO · 6Al₂O₃. *Neues Jahrb. Mineral. Abh.* **109**, 192–200.

Keil K. and Fuchs L. H. (1971) Hibonite [$Ca_2(Al, Ti)_{24}O_{38}$]from the Leoville and Allende chondritic meteorites. *Earth Planet. Sci. Lett.* **12**, 184–190.

Kemper F., Jaeger C., and Waters L. B. F. M. (2002) Detection of carbonates in dust shells around evolved stars. *Nature* **415**, 295–297.

Lodders K. (2003) Solar system abundances and condensation temperatures of the elements. *Astrophys. J.* **591**, 1220–1247.

Lodders K. and Fegley B. (1999) Condensation chemistry of circumstellar grains. In *Asymptotic Giant Branch Stars* (eds. T. Le Bertre, A. Lebre, and C. Waelkens) pp. 279–289, Astronomical Society of the Pacific, San Francisco, CA.

MacPherson G. J., Davis A. M., and Zinner E. K. (1995) 26-Aluminum in the early solar system: A reappraisal. *Meteoritics* **30**, 365–386.

Mayerhöfer T. G. (2002) New method of modeling infrared spectra of non-cubic single-phase polycrystalline materials with random orientation. *Appl. Spectros.* **56**, 1194–1205.

McAloon B. P. and Hofmeister A. M. (1993) Symmetry of birefringent garnets from infrared spectroscopy. *Am. Miner.* **78**, 957–967.

Moine B., Rakotondrazafy M., Ramambazafy A., Rakotondratsima C., and Cuney M. (1997) Proceedings of the UNESCO-IUGS-IGCP International Field Workshop on Proterozoic Geology of Madagascar. Controls on the urano-thorianite deposits in S-E Madagascar, pp. 55–56.

Molster F. J., Lim T. L., Sylvester R. J., Waters L. B. F. M., Barlow M. J., Beintema D. A., Cohen M., Cox P., and Schmitt B. (2001) The complete ISO spectrum of NGC 6302. *Astron. Astrophys.* **372**, 165–172.

Murakami T., Chakoumakos B. C., Ewing R. C., Lumpkin G. R., and Weber W. J. (1991) Alpha-decay event damage in zircon. *Am. Miner.* **76**, 1510–1532.

Mutschke H., Posch T., Fabian D., and Dorschner J. (2002) Towards the identification of circumstellar hibonite. *Astron. Astrophys.* **392**, 1047–1052.

Nasdala L., Irmer G., and Wolf D. (1995) The degree of metamictization in zircon: A Raman spectroscopic study. *Eur. J. Mineral.* **7**, 471–478.

Nittler L. R., Alexander C. M. O'D., Gao X., Walker R. M., and Zinner E. K. (1994) Interstellar oxide grains from the Tieschitz ordinary chondrite. *Nature* **370**, 443–446.

Palmer D. C. (1994) Stuffed derivatives of the silica polymorphs. *Rev. Miner.* **29**, 83–122.

Paque J. M. (1987) CaAl$_4$O$_7$ from Allende Type A inclusion NMNH 4691. *Lunar Planet. Sci.* XVIII, 762–763.

Pezzota F, Simmons W. B., (2001) Field Course on the Rare Element Pegmatites of Madagascar, Technical Program and Field Trip Guidebook, June 11–22, 2001, Antananarivo, Madagascar.

Podosek F. A. and Cassen P. (1994) Theoretical, observational, and isotopic estimates of the lifetimes in the solar nebula. *Meteoritics* **29**, 6–25.

Ponomarev V. I., Kheiker D. M., and Belov N. V. (1970) Crystal structure of calcium dialuminate, CA$_2$. *Soviet Physics–Crystallography* **15**, 995–998.

Ríos S., Malcherek T., Salje E. H., and Domeneghetti C. (2000) Localized defects in radiation-damaged zircon. *Acta Crystallographica* B56, 947–952.

Salama A., Kessler M. F., Leech K., and Schulz B. (2000) ISO beyond the peaks: The 2nd ISO workshop on analytical spectroscopy, Madrid, Spain, ESA-SP456, Madrid, Spain.

Sloan G. C., Kraemer K. E., Goebel J. H., and Price S. D. (2003) Guilt by association: The 13 micron dust emission feature and its correlation to other gas and dust features. *Astrophys. J.* **594**, 483–495.

Speck A. K. and Hofmeister A. M. (2004) Processing of presolar grains around post-AGB stars: Silicon carbide as the carrier of the "21" micron feature. *Astrophys. J.* **600**, 986–991.

Speck A. K., Barlow M. J., Sylvester R. J., and Hofmeister A. M. (2000) Dust features in the 10-μm infrared spectra of oxygen-rich evolved stars. *Astron. Astrophys. Suppl. Ser.* **146**, 437–464.

Spitzer W. G., Miller R. C., Kleinman D. A., and Howarth L. W. (1962) Far-infrared dielectric dispersion in BaTiO$_3$, SrTiO$_3$, and TiO$_2$. *Phys. Rev.* **126**, 1710–1721.

Stebbins J. F., Oglesby J. V., and Kroeker S. (2001) Oxygen triclusters in crystalline CaAl$_4$O$_7$ (grossite) and in calcium aluminosilicate glasses: ^{17}O NMR. *Am. Miner.* **86**, 1307–1311.

Sulewski P. E., Noh T. W., McWhirter J. T., and Sievers A. (1987) Far-infrared composite-medium study of sintered La$_2$NiO$_4$ and La$_{1.85}$Sr$_{0.15}$CuO$_{4-y}$. *Phys. Rev. B* **36**, 5735–5738.

Utsunomiya A., Tanaka K., Morikawa H., Marumo F., and Kojima H. (1988) Structure refinement of CaO.6Al$_2$O$_3$. *J. Solid State Chem.* **75**, 197–200.

Waters L. B. F. M. (2000) The life cycle of dust: An ISO view. In *ISO Beyond the Peaks: The 2nd ISO Workshop on Analytical Spectroscopy* (eds. A. Salama, M. F. Kessler, K. Leech and B. Schulz), pp. 39–48, European Space Agency, Madrid, Spain.

Weber D. and Bischoff A. (1994) Grossite (CaAl$_4$O$_7$)—a rare phase in terrestrial rocks and meteorites. *Eur. J. Mineral.* **6**, 591–594.

Weber W. J., Ewing R. C., and Wang L. M. (1994) The radiation-induced crystalline-to-amorphous transition in zircon. *J. Mater. Res.* **9**, 688–698.

Woodhead J. A., Rossman G. R., and Silver L. T. (1991) The metamictization of zircon: Radiation dose-dependent structural characteristics. *Am. Miner.* **76**, 74–82.

Wooten F. (1972) *Optical Properties of Solids.* Academic Press, San Diego.

Wopenka B., Jolliff B. L., Zinner E., and Kremser D. T. (1996) Trace element zoning and incipient metamictization in a lunar zircon: Application of three microprobe techniques. *Am. Miner.* **81**, 902–912.

APPENDIX

Spectral files to accompany this paper are available as electronic annexes (E1-E9; Elsevier, Science Direct).

"CaA1O4merge.txt" is tab delimited text of the merged spectra of synthetic CaA12O4 in Figure 3a. The left column is the frequency in wavenumbers. The right column is the chemical absorbance (common logarithm based). The thickness of the sample is no more than 3 micron; see text section 5.2 for discussion.

"Grosmerge.txt" is tab delimited text of the merged spectra of synthetic grossite in Figure 3b. Pure isotopically normal sample was used except for the interval of 300 to 500 cm^{-1}, where the 17 O enriched sample was used. The left column is the frequency in wavenumbers. The right column is the chemical absorbance (common logarithm based). The thickness of the sample is no more than 0.4 micron, see text section 5.2 for discussion.

"hibsynmerge.txt" is tab delimited text of the merged spectra of synthetic hibonite in Figure 3c. The left column is the frequency in wavenumbers. The right column is the chemical absorbance (common logarithm based). The thickness of the sample is no more than 2.2 micron, see text section 5.2 for discussion.

"CaOmerge.txt" is tab delimited text of the merged spectra of synthetic, dried CaO in Figure 3d. The left column is the frequency in wavenumbers. The right column is the chemical absorbance (common logarithm based). The thickness of the sample is no more than 2.2 micron, see text section 5.2 for discussion.

"corsynmerge.txt" is tab delimited text of the merged spectra of synthetic corundum in Figure 3d. The left column is the frequency in wavenumbers. The right column is the chemical absorbance (common logarithm based). The thickness of the sample is 0.45 micron, see text section 5.2 for discussion.

"hibnatkramers.txt" is tab delimited text of the merged reflectance spectra of natural hibonite, E perpendicular to c, and its Kramers-Kronig analysis. From left to right, columns are: frequency, real part of dielectric function, imaginary part of dielectric function, imaginary part of 1/dielectric function, reflectivity (0-1), absorption coefficient (1/cm), n, k, conductivity. Only the frequency column has units (1/cm). The data are shown in Fig. 4. Above about 1200 cm^{-1}, the data have interference fringes.

"farIRminerals.txt" is tab delimited text of the far-IR data in Figure 6. The three columns are from left to right, mineral name, frequency, chemical absorbance. From top to bottom, the minerals are forsterite, diopside, enstatite, akermanite, gehlenite, melilite. Film thickness is about 1 micron.